Syngap1 regulates the synaptic drive and membrane excitability of Parvalbumin-positive interneurons in mouse auditory cortex

Ruggiero Francavilla[1,2], Bidisha Chattopadhyaya[1], Jorelle Linda Damo Kamda[1,2], Vidya Jadhav[1,2], Saïd Kourrich[3,4,5], Jacques L. Michaud[1,2,6], Graziella Di Cristo[1,2,#]

1.CHU Sainte-Justine Azrieli Research Centre, 3175 Côte Ste-Catherine, Montreal, Quebec, Canada H3T 1C5. 2. Department of Neurosciences, Université de Montréal, C.P. 6128, Succ. Centre-Ville, Montreal, Quebec, Canada H3C 3J7. 3. Département des sciences biologiques, UQAM, 141 Av. du Président-Kennedy, Montréal, QC H2X 1Y4, Canada. 4. Centre d'Excellence en Recherche sur les Maladies Orphelines-Fondation Courtois, Pavillon des Sciences biologiques, 141 Avenue du Président-Kennedy, Montréal, QC H2X 3Y7, Canada. 5. Center for Studies in Behavioral Neurobiology, Concordia University, Montreal, QC H4B 1R6, Canada. 6. Department of Pediatrics, Université de Montréal, C.P. 6128, Succ. Centre-Ville, Montreal, Quebec, Canada H3C 3J7.

Corresponding author: graziella.di.cristo@umontreal.ca

Abstract

SYNGAP1 haploinsufficiency-related intellectual disability (SYNGAP1-ID) is characterized by moderate to severe ID, generalized epilepsy, autism spectrum disorder, sensory processing dysfunction and other behavioral abnormalities. While most studies, so far, have focussed on the role of Syngap1 in cortical excitatory neurons, recent studies suggest that Syngap1 plays a role in GABAergic inhibitory neuron development as well. However, the molecular pathways by which Syngap1 acts on GABAergic neurons, and whether they are similar or different from the mechanisms underlying its effects in excitatory neurons, is unknown. Here we examined whether, and how, embryonic-onset *Syngap1* haploinsufficiency restricted to GABAergic interneurons derived from the medial ganglionic eminence (MGE) impacts their synaptic and intrinsic properties in adulthood. We found that *Syngap1* haploinsufficiency affects the intrinsic properties, overall leading to increased firing threshold, and decreased excitatory synaptic drive of Parvalbumin (PV)+ neurons from Layer IV auditory cortex in adult mice, whilst Somatostatin (SST)+ interneurons were mostly resistant to *Syngap1* haploinsufficiency. Further, the AMPA component of thalamocortical evoked-EPSC was decreased in PV+ cells from mutant mice. Finally, we found that targeting the Kv1 family of voltage-gated potassium channels was sufficient to rescue PV+ mutant cell-intrinsic properties to wild-type levels. Together, these data suggest that *Syngap1* plays a specific role in the maturation of PV+ cell intrinsic properties and synaptic drive, and its haploinsufficiency may lead to reduced PV cell recruitment in the adult auditory cortex, which could thus underlie the auditory processing alterations found in SYNGAP1-ID preclinical models and patients.

Introduction

In mammals, the ability of the brain to process, perceive and integrate sensory stimuli is an essential function. Among the sensory modalities, audition is crucial for communication and perception of threats, which involves detecting sudden changes in the acoustic environment and extracting relevant acoustic features from noise. For mice, auditory navigation and assessment is based on the auditory system's capacity to detect, separate, and analyse spectro-temporal information from the acoustic environment (King et al., 2018). In the mammalian primary auditory cortex (A1), neurons are well tuned to specific sound frequency, intensity, or repetition rate (Kilgard and Merzenich, 1999, Schreiner et al., 2007). Interestingly, A1 neurons also exhibit adaptation, attenuating their responses to redundant, repetitive stimuli carrying non-relevant information (Ulanovsky et al., 2003; Szymanski et al., 2009). Such auditory computations are carried out by cortical circuits composed of tightly coupled networks of excitatory and inhibitory neurons.

GABAergic inhibitory neurons play a pivotal role in auditory circuits shaping cortical activity and modulating auditory information processing (Wehr and Zador, 2003). Based on anatomical, physiological and specific marker expression, we can identify two major sub-classes of cortical inhibitory neurons, parvalbumin- (PV+) and somatostatin- (SST+) expressing interneurons, which provide perisomatic and distal dendritic inhibition to pyramidal cells (PCs), respectively (Reyes and Levy, 2012; Yavorska and Wehr, 2016) in the auditory cortex. Due to the specificity in their synapse location and distinct functional properties, SST+ and PV+ neurons differentially shape excitatory neuronal responses. By providing fast inhibition onto postsynaptic PC cell somata and proximal dendrites, PV+ cells exert fine control on their output (Moore and Wehr, 2013; Tremblay et al., 2016), while SST+ cells targeting apical dendrites of postsynaptic PCs exert specific control over dendritic synaptic integration (Kawaguchi and Kubota, 1997; Chiu et al., 2013). In recent years, novel transgenic and optogenetic technologies have allowed for precise labeling and manipulation of these two major classes of GABAergic interneurons *in vivo* in order to address their specific role

in auditory processing and sound perception (Letzkus et al., 2011; Pi et al., 2013; Hamilton et al., 2013; Keller et al., 2018; Ceballo et al., 2019; Chai et al., 2022; Nocon et al., 2023). Specifically, SST+ neurons have a dominant role in the integration of information across multiple auditory frequencies and respond relatively slowly to a narrower range of tones (Lakunina et al., 2020; Li et al., 2015). In contrast, the role of PV+ cells in auditory processing is still controversial with some studies reporting PV+ cells activated by a broad set of tones (Cohen and Mizrahi 2015; Li et al., 2015) and others showing they are well-tuned for specific auditory frequencies (Moore and Wehr 2013; Aizenberg et al., 2015; Christensen et al., 2019). The variability in the recruitment of PV+ cells remains a caveat in optogenetic studies performed in the auditory cortex (Seybold et al., 2015; Phillips and Hasenstaub, 2016; Keller et al., 2018; Gothner et al., 2021) making data interpretation difficult. A possible explanation for the heterogeneity in PV+ cell recruitment could be the presence of discrete subtypes within PV+ expressing neurons, as suggested by recent single cell transcriptomics data (Bakken et al., 2021; Zhang et al., 2021). Further, while GABAergic interneurons have been extensively studied in other cortical areas, there are relatively few reports on PV+ and SST+ cell-intrinsic and synaptic properties in adult auditory cortex (Chen et al., 2015; Rock et al., 2018; Wang et al., 2022; Henton et al., 2023).

Abnormalities in auditory sensory processing are common in patients with autism spectrum disorder (ASD) and are hypothesized to contribute to core ASD behaviors (Gonçalves and Monteiro, 2023). However, the neurobiological basis of abnormal auditory processing and how it develops is still unclear (Sinclair et al., 2017). Here, we focus on an increasingly well-recognised candidate gene in neurodevelopmental disorders, *Syngap1*, haploinsufficiency of which causes intellectual disability (SYNGAP1-ID), epilepsy, and autistic features (Hamdan et al., 2009; Berryer et al., 2013). Further, *Syngap1* haploinsufficient mouse models and SYNGAP1-ID patients show similar changes in auditory processing, including increased baseline and evoked gamma oscillatory activity and impaired habituation to repetitive stimuli (Carreño-Muñoz et al., 2022). These specific

alterations are recapitulated in a mouse model where *Syngap1* haploinsufficiency is restricted to neurons derived from the medial ganglionic eminence (MGE), which include cortical PV+ and SST+ interneurons (Jadhav et al, in preparation), which suggests that GABAergic cell-specific dysfunction has a role in sensory processing alterations observed in preclinical models and SYNGAP1-ID patients; however, the underlying neurobiological mechanisms remains to be elucidated.

The function of *Syngap1* has been mostly studied in excitatory neurons; in particular, *Syngap1* haploinsufficiency has been shown to increase AMPA receptor density and cause premature maturation of excitatory synapses formed by hippocampal and layer 5 pyramidal cells in the somatosensory cortex (Clement et al., 201, 2013; Ozkan et al., 2014; Aceti et al, 2015). Further, *Syngap1* can play a non-synaptic function linked to the control of cortical neurogenesis of projecting neurons (Birtele et al., 2023). Recent studies have implicated *Syngap1* in GABAergic cell migration and inhibitory synapse maturation (Berryer et al., 2016; Su et al., 2019; Sullivan et al., 2020; Khlaifia et al., 2023); nevertheless, whether the underlying cellular and molecular mechanisms are similar to those observed in excitatory cells is unknown.

We generated conditional transgenic mice wherein *Syngap1* haploinsufficiency was restricted to MGE-derived interneurons. We then assessed the synaptic and intrinsic properties of PV+ fast spiking (FS) and SST+ regular spiking cells in layer IV of the adult auditory cortex. We performed whole-cell voltage clamp recording in combination with electrical stimulation of thalamic fibers and current clamp recording, to study synaptic and intrinsic properties, respectively. We found that both mutant PV+ and SST+ cells show decreased excitatory synaptic drive; however, PV+, but not SST+, interneurons showed significantly increased threshold for action potential generation, which points towards a reduced recruitment of cortical PV cells in the mutant mouse. Further, we rescued PV+ cell hypofunction ex vivo using alpha-dendrotoxin (α-DTX), a drug specifically targeting the Kv1 family of voltage-gated potassium channels, suggesting that Syngap1 can act by modulating

distinct molecular factors in a cell-specific fashion. Altogether our results highlight the importance of dissecting cell type-specific changes caused by *Syngap1* haploinsufficiency.

RESULTS

Syngap1 haploinsufficiency in MGE-derived interneurons is associated with network-dependent decrease of synaptic excitation and inhibition in PV+ cells

Since *Syngap1* has been shown to regulate AMPAR-mediated synaptic transmission in hippocampal cortical excitatory neurons and hippocampal inhibitory neurons (Ozkan et al., 2014; Arora et al., 2022; Khlaifia et al., 2023), we first explored whether embryonic-onset *Syngap1* haploinsufficiency in MGE-derived interneurons affects glutamatergic synaptic inputs to Nkx2.1+ interneurons from adult layer IV (LIV) auditory cortex, using whole cell voltage clamp recordings of spontaneous (sEPSCs) and miniature excitatory postsynaptic potentials (mEPSCs) (***Figure 1a–j, Figure supplement 1a-e, Table 1, Table S1***). Nkx2.1-expressing MGE precursors generate most of PV+ and SST+ cortical interneurons (Xu et al., 2008). Recorded MGE-derived interneurons, identified by GFP expression, were filled with biocytin, followed by *posthoc* immunolabeling with anti-PV and anti-SST antibodies. PV+ and SST+ interneuron identity was confirmed using neurochemical marker (PV or SST) expression and anatomical properties (axonal arborisation location, presence of dendritic spines). We found that sEPSC amplitude, but not inter-event interval, was decreased in both LIV PV+ and SST+ neurons from Tg(*Nkx2.1-Cre*):*RCE*$^{f/f}$:*Syngap1*$^{+/+}$ (control) and Tg(*Nkx2.1-Cre*):*RCE*$^{f/f}$:*Syngap1*$^{f/+}$ (cHet) littermates (***Figure 1b, Figure supplement 1b***). sEPSC rise and decay time constants for both PV+ and SST+ interneurons was not significantly different between the two genotypes (***Figure 1d, Figure supplement 1d***), suggesting that postsynaptic AMPA receptor subunit composition was not affected by *Syngap1* haploinsufficiency. Finally, charge transfer (area under sEPSC) and the product of mean PSC charge transfer and event frequency were both

significantly decreased in SST+, but not PV+ cells in cHet mice compared to controls (***Figure 1e, Figure supplement 1e***). To discern whether *Syngap1* haploinsufficiency had a pre or postsynaptic action on the glutamatergic drive received by PV+ cells, we recorded mEPSC (***Figure 1f-j***). We found no difference in mEPSC amplitude between the two genotypes (Fig. 1g), indicating that the observed difference in sEPSC amplitude (***Figure 1b***) could arise from decreased network excitability. Conversely, cHet mice showed a shift toward an increase in the inter-mEPSC time interval (***Fig. 1g***). Consistent with this observation, we observed a significant decrease in the density of putative glutamatergic synapses onto PV+ cell somata, identified by the colocalization of the vesicular glutamate 1 (vGlut1, presynaptic marker) and PSD95 (postsynaptic marker), in cHet compared to control mice (***Figure 1, Figure supplement 2a, b***). All together these data suggest that cHet PV+ cells have a reduced glutamatergic drive as compared to control PV+ cells.

Since PV+ cell recruitment is regulated by the balance of its excitatory and inhibitory inputs, we next analysed sIPSC and mIPSC from layer IV PV+ cells in both genotypes. We observed reduced sIPSC amplitude, but no significant changes in frequency and kinetics, in cHet compared to control PV+ cells (***Figure 2a-e, Table 2***). However, mIPSC analysis revealed no genotype-dependent differences in any parameters (***Figure 2a-j, Table 2***), suggesting that decreased sIPSC amplitude in cHet PV+ cells was likely due to changes in presynaptic cell-intrinsic excitability and/or network activity.

Embryonic-onset *Syngap1* haploinsufficiency in MGE-derived interneurons attenuate thalamocortical evoked AMPA transmission in layer IV PV+ cells

In A1, layer IV PV+ cells receive intracortical (Kratz and Manis, 2015) and stronger subcortical thalamocortical inputs compared to excitatory cells and other subpopulations of GABAergic interneurons (Ji et al., 2016; Rock et al., 2018). We thus recorded AMPA- and NMDA-mediated currents evoked in PV+ cells by minimal electrical stimulation of the thalamic radiation (***Figure 3a-f, Table 3***), to determine whether putative single thalamocortical synapses were affected by

conditional *Syngap1* haploinsufficiency. Minimally evoked AMPA amplitude, AUC charge transfer (average of all responses, successes + failures, ***Figure 3b,c***) and potency (average of all successes only, ***Figure 3e***) were decreased in cHet mice as compared to control littermates. In addition, we found a substantial increase in onset latencies of evoked AMPA currents (***Figure 3d***), suggesting a potential deficit in the thalamocortical recruitment of PV+ cells. Next, we assessed evoked NMDA EPSCs in PV+ cells in presence of $GABA_AR$, $GABA_B$ and AMPA inhibitors (1 μM Gabazine, 2 μM CGP, and 10 μm NBQX, respectively) (***Figure 3c,e***). We found that evoked NMDA currents as well as the percentage of PV+ cells showing these responses were similar in cHet and control littermates (***Figure 3c,e***), therefore leading to increased NMDA/AMPA in cHet mice (***Figure 3e***). Interestingly, the kinetics of evoked AMPA and NMDA currents were similar in both genotypes, indicating no change in their subunit composition (***Figure 3f***). These results suggest that embryonic-onset *Syngap1* haploinsufficiency in MGE-derived interneurons specifically impairs AMPA-mediated thalamocortical recruitment of PV+ cells. Of note, the density of putative thalamocortical glutamatergic synapses onto PV+ cell somata, identified by the colocalization of the vesicular glutamate 2 (vGlut2, thalamocortical presynaptic marker) and PSD95 (postsynaptic marker) was not significantly different in cHet as compared to littermate controls (***Figure 3, Figure Supplement 2c,d***), suggesting that presynaptic release from putative single excitatory thalamocortical fiber or/and AMPARs expression at thalamocortical synapses on PV+ cells are likely decreased in cHet mice.

Layer IV PV+ cells show normal dendritic morphology in *Nkx2.1 Cre$^{+/-}$RCE$^{f/f}$ Syngap1$^{f/+}$* mice

Reduced glutamatergic drive onto PV+ cells may be due to impaired dendritic development. Since *Syngap1* haploinsufficiency has been shown to impact the dendritic arbor of glutamatergic neurons (Clement et al., 2012; Michaelson et al., 2018; Arora et al., 2022), we next asked whether embryonic-onset conditional *Syngap1* haploinsufficiency in PV+ cells had similar effects. We reconstructed the full dendritic arbor of PV+ cells filled with biocytin during patch-clamp

recordings followed by *posthoc* immunolabeling with anti-PV and anti-SST antibodies (***Figure 4a-c, Table 4***). We observed that PV+ cells had an ovoid somata and multipolar dendrites typical of the basket cell (BC) family (Fig. 4a). We observed no genotype-dependent differences in soma perimeter, number of branching points, total dendritic length and total dendritic area (***Figure 4b***). Further, dendritic Sholl analysis revealed no differences in dendritic intersections at different distances from the soma (***Figure 4c***). Together, these data indicate that in contrast to observations in cortical glutamatergic neurons (Clement et al., 2012; Michaelson et al., 2018; Arora et al., 2022), embryonic-onset *Syngap1* haploinsufficiency in PV+ cells did not alter their dendritic arborisation. Therefore, structural modifications cannot explain the observed reduction in their glutamatergic drive (***Figure 1 a-j***).

cHet mice show decreased layer IV PV+ cell-intrinsic excitability

PV+ cell recruitment in cortical circuits is dependent on both their synaptic drive and intrinsic excitability. Thus, we sought to investigate how *Syngap1* haploinsufficiency in MGE-derived interneurons impacts the intrinsic excitability and firing properties of PV+ cells, by performing whole-cell current clamp recordings (***Figure 5a-e, Table 5***). In line with preserved neuronal morphology, we found no changes in passive membrane properties (Cm, Rin and τ) of PV+ cells recorded from cHet mice as compared to control littermates (***Figure 5a***). However, analysis of active membrane properties revealed a significant decrease in the excitability of mutant PV+ cells (***Figure 5b,c***). In particular, cHet PV+ cells showed reduced AP amplitude and increased AP threshold and latency to first AP (***Figure 5b,c***), while overall AP kinetics, including AP rise and decay time, fAHP time and AP half width were not affected (***Figure 5b, Table 5***). In line with the decrease in intrinsic excitability, the rheobase (the smallest current injection that triggers an AP) was increased in PV+ cells from cHet mice (***Figure 5d***). In addition, both cHet and control PV+ cells displayed typical, sustained high-frequency trains of brief APs with little spike frequency adaptation in response to incremental current injections (***Fig. 5e, right***). However, cHet PV+

interneurons fired fewer APs in response to the same depolarizing current injection when compared to control mice (***Figure 5e, left***). These data show that embryonic-onset *Syngap1* haploinsufficiency in PV+ cells impairs their basic intrinsic and firing properties.

Embryonic-onset *Syngap1* haploinsufficiency in MGE-derived interneurons differentially affects the dendritic arbor and intrinsic properties of two distinct PV+ cell subpopulations

The majority of PV+ cells are classified as fast-spiking (FS) cells, due to their ability to sustain high-frequency discharges of APs (***Figure 5e, right***). However, clusters of atypical PV+ cells have been previously reported in several brain regions including subiculum (Nassar et al., 2015), striatum (Bengtsson Gonzales et al., 2020), hippocampus (Ekins et al., 2020) and somatosensory cortex (Helm et al., 2013). Atypical PV+ cells share many electrophysiological parameters with FS cells; however, they have a slower half width and possess a lower maximal AP firing frequency (Nassar et al., 2015; Bengtsson Gonzales et al., 2018; Ekins et al., 2020; Helm et al., 2013). Based on these 2 criteria, in our data we found a strong negative correlation between F_{max}initial and AP half-width in both genotypes (***Figure 6a, left***), indicating the possible existence of PV+ cell subgroups in both cHet and control mice. To verify whether auditory cortex PV+ cells from control mice could be functionally segregated into distinct clusters, we performed hierarchical clustering of AP half-width and F_{max} values based on Euclidean distance (***Figure 6a, right***). Hierarchical clustering builds a map (dendrogram) quantifying the similarity between samples (PV+ cell) and clusters of samples. Based on this analysis, we identified 2 clusters of PV+ cells, with short AP half-widths associated with higher values of F_{max}. Despite hierarchical clustering defining 2 subgroups of PV+ cells, there were still few PV+ cells with longer AP half-widths showing F_{max} values typical of shorter AP half-widths (***Figure 6a, right***). We thus decided to perform PCA analysis using additional key intrinsic physiological features such as passive (V_m, R_{in}, C_m) and active (rheobase, AP half-width, AP amplitude, first AP latency, AP threshold, fAHP amplitude, amplitude AR, frequency AR, F_{max} and F_{ss}) membrane properties (***Figure 6b, left***). We then chose the intersection point of the 2 AP half-

width distributions in control and cHet mice as a cutoff to define 2 different subpopulations of PV+ cells, which we termed Basket Cell (BC)-short (AP half-width <0.78ms) and BC-broad (AP half-width ≥0.78ms) (***Figure 6c,d***). In control mice, these 2 PV+ cell subtypes showed major differences in R_{in}, C_m, F_{max} and F_{ss} (Table S2, comparison between BC-short and BC-broad in control mice). Using PCA analysis we also noticed that, while in control mice we could clearly distinguish 2 PV+ cell subgroups, the differences were more ambiguous in cHet mice wherein some BC-short felt in the subdivision of BC-broad (***Figure 6d***). In addition, we observed that the percentage of BC-short was increased in cHet compared to control mice (61% vs 41% of total PV+ cells, respectively), suggesting that *Syngap1* haploinsufficiency affects specific subgroups of PV+ cells (***Figure 6d***).

Next, we examined whether the diversity in PV+ cell electrophysiological profiles was reflected in their dendritic arborisation (***Figure 6e-h, Table 6.1, 6.2, 6.3, 6.4***). Somata anatomical location (distance in μ from pia) was quantified as well to confirm that the recorded and analysed cells were located in LIV (***Figure 6g,h***). In control mice, both BC-short and BC-broad cells showed ovoid somata and multipolar dendrites (***Figure 6e,f***). Anatomical reconstruction and morphometric analysis revealed differences in dendritic arborization that correlated positively with AP half-width in control mice (***Figure 6g,k***). In particular, BC-short cells showed significantly lower branch point numbers and dendritic surface area as compared to BC-broad cells (***Figure 6g***). In contrast, the dendritic arbor of BC-short neurons and BC-broad did not show significant differences in cHet mice (***Figure 6h***). Direct comparison of PV+ cell dendritic arbor in cHet vs control littermates clearly showed that BC-short neurons are specifically affected by *Syngap1* haploinsufficiency (***Figure 6i, j***), with cHet BC-short cells showing a significant increase in dendritic complexity compared to those from control mice (***Figure 6i***). Further, the strong positive correlation of dendritic surface area with AP half-width was present only in PV+ cells from control mice, but disappeared in cHet mice (***Figure 6k***). Altogether, these data indicate that embryonic-onset *Syngap1* haploinsufficiency

in Nkx2.1+ interneurons alters the dendritic development of a specific PV+ cell subpopulation, which could in turn affect their intrinsic excitability and dendritic integration of synaptic inputs.

Based on the observed heterogeneity in morpho-electric parameters of PV+ cells, we next sought to investigate the effect of *Syngap1* haploinsufficiency on the intrinsic excitability of specific PV+ cell subtypes (***Figure 7, Tables 7.1, 7.2***). We found that BC-short cells showed preserved passive membrane properties (Fig. 7a) and altered active membrane properties (***Figure 7b-e***) in cHet compared to control mice. In particular, we found increased AP threshold affecting AP amplitude (***Figure 7b,c***) and increased rheobase current (***Figure 7d***), indicating a decrease in the excitability of cHet BC-short cells. cHet BC-short interneurons displayed AP patterns similar to those in control BC-short (***Figure 7e, right***), but fired less APs in response to somatic depolarization (***Figure 7e, left***). In contrast, BC-broad neurons had a more hyperpolarized RMP (***Figure 7f***), and increased AP latency and threshold (***Figure 7g,h***) in cHet mice compared to controls. However, in cHet BC-broad neurons these changes were not translated into decreased ability to generate spikes (***Figure 7i,j***). Altogether these data suggest that BC-short neurons may be overall more vulnerable to *Syngap1* haploinsufficiency than BC-broad neurons. They further indicate that *Syngap1* levels appears to play a common role in determining the threshold for AP generation in all adult PV+ cells.

SST+ interneuron intrinsic and firing properties are less affected by *Syngap1* haploinsufficiency in MGE-derived interneurons as compared to PV+ cells

Next, we examined whether *Syngap1* haploinsufficiency in MGE-derived interneurons affects the other major group of Nkx2.1-expressing cortical interneurons, the SST+ interneurons (***Figure 8 a-f, Table 8***). In current-clamp recordings, control SST+ cells displayed a low discharge rate and typical AP frequency accommodation in response to incremental steps of current injection (***Figure 8a***). The molecular identity of this interneuron subtype was then confirmed by immunopositivity for SST+ and immunonegativity for PV (***Figure 8b***). Interestingly, PCA analysis using the previously mentioned electrophysiological parameters clearly distinguished SST+ neurons from BC-short

subtype of PV+ cells, but showed an overlap between BC-broad PV+ and SST+ cells (***Figure 8c***). These data indicate that, in mature auditory cortex, a subtype of PV+ cells share some electrophysiological features with SST+ cells, indicating the necessity to perform post-hoc immunohistochemical validation (***Figure 8b,c***). cHet SST+ cells showed no significant changes in active and passive membrane properties (***Figure 8d,e***); however, their evoked firing properties were affected with fewer APs generated in response to the same depolarizing current injection compared to control SST+ cells (***Figure 8f***).

Thus, embryonic-onset *Syngap1* haploinsufficiency in MGE-derived interneurons substantially reduced the excitability of auditory cortex LIV PV+ and SST cells, with a major impact on the PV+ cell population as reflected in both single AP properties and AP firing pattern.

A selective Kv1-blocker rescues PV+ cell intrinsic excitability in cHet mice

Based on previous studies performed in PV+ cells (Wang et al., 1994; Goldberg et al., 2008; Zurita et al., 2018), changes in the Kv1 family of voltage-gated potassium channel could account for the observed altered intrinsic excitability observed in cHet mice. To test this hypothesis, we performed current clamp recordings from PV+ cells in control and cHet mice in presence or absence of α-DTX (100 nM), a specific blocker of channels containing Kv1.1, Kv1.2 or Kv1.6 (***Figure 9a-e, Table 9***). As hypothesized, the presence of α-DTX rescued the voltage threshold for AP generation in cHet PV+ cells to control levels, without affecting the AP shape parameters (***Figure 9b,c, Table 9***), while the relation between the number of action potntials and current injection remained the same (***Figure 9d***), indicating that α-DTX had no impact on PV+ cell firing. Further, α-DTX facilitated AP initiation in cHet PV+ cells by reducing AP delay from stimulation onset (***Figure 9e***). Also, α-DTX-treated cHet PV+ cells were indistinguishable from controls, treated with either vehicle or α-DTX (***Figure 9e***). These data revealed that *Syngap1* haploinsufficiency potentially affects the activity of Kv1 family of voltage gated potassium channel, thereby decreasing the excitability of PV+ cells in adult auditory cortex.

DISCUSSION

In this study, we dissected the circuit basis of abnormal cortical auditory function in embryonic-onset MGE-restricted *Syngap1* haploinsufficient mice. Our data demonstrated that in auditory cortex, PV+ cells are particularly vulnerable to *Syngap1* haploinsufficiency. In particular, mutant PV+ cells showed reduced intracortical and thalamo-cortical synaptic drive, contrary to *Syngap1*'s documented role in the formation and plasticity of glutamatergic synapses on excitatory cells. We further found that *Syngap1* haploinsufficiency alters PV+, but not SST+, cell intrinsic properties, overall leading to decreased intrinsic excitability affecting its input-output function. PV+ cell intrinsic excitability was rescued by pharmacological inhibition of Kv1 containing K+ channels, indicating their potential involvement as molecular mediators of functional deficits induced by *Syngap1* haploinsufficiency. *Syngap1* has been studied mainly in the context of synaptic physiology; therefore, our data highlights a novel aspect of *Syngap1* biology.

Syngap1 is thought to be a potent regulator of excitatory synapses and its reduced expression in excitatory cells causes an increase in AMPA receptor density and premature maturation of excitatory synapses (Rumbaugh et al., 2006; Clement et al., 2012; 2013). Unexpectedly, here we found that the *Syngap1* haploinsufficiency in MGE-derived interneurons depresses AMPA-mediated synaptic transmission based on a potential presynaptic mechanism involving the reduction of glutamatergic boutons. Further, LIV PV+ cells receive the strongest thalamocortical input compared to excitatory cells and other subpopulation of GABAergic interneurons (Ji et al., 2016; Zurita et al., 2018). Our study showed that one of the sources of the deficit in glutamatergic drive arises from a decrease in the AMPA-mediated thalamocortical input reaching PV+ cells, suggesting a decrease in presynaptic release from putative single excitatory thalamocortical fiber and/or reduction in AMPARs expression at these synapses in cHet mice. Interestingly our data showed increased onset latencies of thalamocortical evoked AMPA together with enhanced NMDA/AMPA ratio, indicating

a kinetically slower thalamic recruitment of PV+ cells. How could *Syngap1* haploinsufficiency in Nkx2.1-expressing cells affect the glutamatergic drive coming from local and thalamic excitatory cells? Here, we showed a novel role of *Syngap1* in promoting GABAergic cell intrinsic excitability, particularly in cortical PV+ interneurons. These findings are in line with recent data reporting a decrease in intrinsic excitability of developing cortical excitatory cells (Arora et al., 2022), and highlight the emerging function of *Syngap1* in the somato-dendritic compartment (Arora et al., 2022). Since in PV+ cells, connectivity and cell excitability are reciprocally regulated at the circuit level (Favuzzi et al., 2017), it is possible that early-onset *Syngap1* haploinsufficiency in MGE-derived interneurons may first affect the development of their intrinsic excitability properties, which in turn would modulate the maturation of their excitatory drive, and activity levels in adulthood. Alternatively, homeostatic adaptation of PV+ interneurons in response to the decreased number of excitatory inputs could trigger changes in Kv1 channels (Dehorter et al., 2015; Favuzzi et al., 2017). Therefore, *Syngap1* may play complex roles at the cellular level and at different developmental stages, based on the crosstalk between neuronal activity levels and Syngap1 localisation and interaction with other proteins.

Based on morphology and synaptic targets, 3 main subgroups of PV+ cells have been identified in auditory cortex, ie basket cells (BCs), chandelier cells and long-range projecting PV+ cells (Levy and Reyes, 2012, Roch et al., 2018; Zurita et al., 2018; Bertero et al., 2019). Despite differences in morphology and target selectivity, different PV+ cell subgroups share common electrophysiological features such as short AP-half width, low input resistance, very high rheobase, and relatively small AP amplitude. In particular, while clusters of atypical BC PV+ have been previously reported in several areas (Helm et al., 2013; Nassar et al., 2015; Bengtsson Gonzales et al., 2018; Ekins et al., 2020), auditory cortex PV+ BCs have been considered as a homogeneous electrophysiological group (Studer and Barkat, 2022). One of the main findings of this study is that mature primary auditory cortex contains at least 2 morphological and electrophysiological subgroups of PV+ BCs,

including a subgroup with a surprising broader duration in AP half-width (Table S2). It is possible that the genetic tools used to identify PV+ cells (*PV_Cre* or G42 mice vs *Nkx2.1*_Cre mice) might enrich for a specific PV+ BC cell subtype. Alternatively, the proportion of different PV+ BCs might depend on the specific cortical region and layer. The presence of at least 2 different PV+ BC cell subtypes with different electrophysiological signatures may in part explain the previously reported variability in the recruitment of auditory cortex PV+ cells in vivo (Seybold et al., 2015; Phillips and Hasenstaub, 2016; Keller et al., 2018; Gothner et al., 2021), since differences might arise from the duration of AP half-width used to sort fast-spiking cells.

Despite the differences observed in how *Syngap1* haploinsufficiency affects the anatomy and physiological properties of the 2 PV+ cell subtypes, a shared deficit we observed was the decrease in intrinsic excitability, as suggested by the increased AP threshold affecting AP initiation. In PV+ cells, the Kv1 family of voltage-gated potassium channels are mainly responsible for AP generation, making them powerful targets to modify AP latency, threshold and rheobase current in these cells (Wang et al., 1994; Goldberg et al., 2008; Zurita et al., 2018). Here, we rescued the excitability of mutant PV+ cells by pharmacologically inhibiting the Kv1 family of voltage gated potassium channels. Consistent with our findings, Arora et al. (2022) rescued pyramidal cell intrinsic excitability and neuronal morphology via lowering elevated potassium channels, by expressing a dominant negative form of the Kv4.2 potassium channel subunit, dnKv4.2, in developing *Syngap1* mutant mice. Kv4.2 and Kv1 potassium channels modulate the intrinsic excitability of pyramidal cell and PV+ interneurons, respectively, indicating that the action of *Syngap1* on potassium channels may be a general mechanism.

A recent study focusing on the PSD interactomes of Syngap1 isolated from adult homogenized mouse cortex suggested a physical interaction between Syngap1 and the potassium channel auxiliary subunit Kvβ2 (Wilkinson and Coba, 2017). Since Kvβ2 regulates the translocation of Kv1 channels in dopaminergic neurons and potentially PV+ cells (Okaty et al., 2009; Yee et al., 2022), it

is possible that *Syngap1* haploinsufficiency may lead to dysregulated Kv1 translocation at the membrane, leading to excessive K currents. Of note, both Kv1 channels and Syngap1 are developmentally regulated (Okaty et al., 2009; Gamache et al., 2020), thus *Syngap1* hypofunction may lead to dysregulation of genes encoding voltage-gated potassium channel affecting cell maturation and excitability.

Interestingly, in cHet SST+ cells, we did not observe deficits in intrinsic excitability, but we found a reduction in number of APs generated at different somatic current injection. The fact that we observed differences in spiking activity in absence of intrinsic excitability alterations, could be due to the heterogeneity of SST+ interneurons likely present in our dataset (Scala et al., 2019; Hostetler et al., 2023). Recent studies showed that SYNGAP1 interacts with Kv4 (Wilkinson and Coba, 2017). Further, *Syngap1* haploinsufficiency leads to increased Kv4 function in pyramidal cells in somatosensory cortex (Arora et al. 2022). Since somato-dendritic Kv4 channels in SST+ interneurons contribute to the regulation of their firing (Serôdio and Rudy, 1998; Bourdeau et al., 2007), *Syngap1* haploinsufficiency might affect SST+ cell excitability via this channel.

PV+ cells have a fundamental role in generating and maintaining gamma oscillations in the brain (Cardin et al., 2009). In particular, recent studies have also shown that deficiency in PV interneuron-mediated inhibition contribute to increased baseline cortical gamma rhythm (Spencer, 2012; Carlén et al., 2012), a phenotype we observed in the auditory cortex of both mutant mice and SYNGAP1-ID patients (Carreño-Muñoz et al., 2022). Specifically, PV+ interneurons, which target the perisomatic domain of pyramidal neurons, are adapted for fast synchronization of network activity controlling spike timing of the excitatory network in auditory cortex (Wehr and Zador, 2003; Li et al. 2014). To sharpen the tuning of neighboring pyramidal cells, PV+ interneurons need to be more effectively recruited by excitatory inputs so that they can restrict the temporal summation of excitatory responses of their pyramidal cell targets and increase the temporal precision of their firing (Povysheva et al., 2006). Our study suggests that decrease in AMPA-

mediated thalamocortical input reaching PV+ cells along with deficits in their intrinsic excitability could account for altered spike timing of pyramidal cells causing an increase in overall network excitability. In our studies, we used a conditional mouse model where *Syngap1* haploinsufficiency is restricted to specific cell types, namely MGE-derived interneurons. Since cell-type specific genetic mutations do not typically occur in humans, it would be interesting to investigate whether *SYNGAP1*-haploinsufficient human-derived neurons show alterations in specific GABAergic subpopulations-intrinsic and synaptic properties.

MATERIALS AND METHODS

Mice

All procedures and experiments were done in accordance with the Comité Institutionnel de Bonnes Pratiques Animales en Recherche (CIBPAR) of the CHU Ste-Justine Research Center in line with the principles published in the Canadian Council on Animal's Care's. Mice were housed (2-5 per cage), maintained in a 12/12 h light/dark cycle, and given ad libitum access to food and water. Experiments were performed in 9-13 weeks-old male mice during the light phase. To investigate the effects of Syngap1 haploinsufficiency in cortical PV+ and SST+ interneurons, we generated mice heterozygous for the Syngap1 conditional allele (*Syngap1*$^{f/f}$; Jackson Laboratories; #029303) under the Tg(*Nkx2.1-Cre*) driver line (Jackson Laboratories; #008661) and further crossed them with mice carrying the RCE allele (Jackson Laboratories; #032037) to generate Tg(*Nkx2.1-Cre*):*RCE*$^{f/f}$:*Syngap1*$^{+/+}$ and Tg(*Nkx2.1-Cre*):*RCE*$^{f/f}$:*Syngap1*$^{f/+}$ mice, for targeted recordings. Nkx2.1-expressing cells were identified by the expression of EGFP.

Acute slice preparation

Briefly, animals were anaesthetized deeply with ketamine–xylazine (ketamine: 100 mg/kg, xylazine: 10 mg/kg), transcardially perfused with 25 mL of ice-cold cutting solution (containing the

following in mM: 250 sucrose, 2 KCl, 1.25 NaH2PO4, 26 NaHCO3, 7 MgSO4, 0.5 CaCl2, and 10 glucose, pH 7.4, 330–340 mOsm/L) and decapitated. The brain was then dissected carefully and transferred rapidly into an ice-cold (0–4 °C) cutting solution. Auditory thalamocortical slices (thickness, 350 μm) containing A1 and the medial geniculate nucleus (MGN) were prepared. For A1 slices, the cutting angle was 15 degrees from the horizontal plane (lateral raised; Cruikshank et al., 2002; Zhao et al., 2009; Meng et al., 2017). Auditory thalamocortical slices were cut in the previously mentioned ice-cold solution using a vibratome (VT1000S; Leica Microsystems or Microm; Fisher Scientific) and transferred to a heated (37.5 °C) oxygenated recovery solution containing the following (in mM): 124 NaCl, 2.5 KCl, 1.25 NaH2PO4, 26 NaHCO3, 3 MgSO4, 1 CaCl2, and 10 glucose; pH 7.4; 300 mOsm/L, and allowed to recover for 45 min. Subsequently, during experiments, slices were continuously perfused (2 mL/min) with standard artificial cerebrospinal fluid (ACSF) containing the following (in mM): 124 NaCl, 2.5 KCl, 1.25 NaH2PO4, 26 NaHCO3, 2 MgSO4, 2CaCl2, and 10 glucose, pH 7.4 saturated with 95% O2 and 5% CO2 at near physiological temperature (30–33°C).

Whole-cell patch clamp recording

PV+ and SST+ neurons located in layer IV of A1 cortex were visually identified as eGFP-expressing somata under an epifluorescence microscope with blue light (filter set: 450–490 nm). All electrophysiological recordings were carried out using a 40x water-immersion objective. Recording pipettes were pulled from borosilicate glass (World Precision Instruments) with a PP-83 two-stage puller (Narishige) to a resistance range of 5–7 MΩ when backfilled with intracellular solution. Whole-cell patch-clamp recordings from PV+ and SST+ interneurons were performed in voltage or current-clamp mode. For voltage-clamp recording, we used an intracellular Cs+-based solution containing (in mM): 130 CsMeSO4, 5 CsCl, 2 MgCl2, 10 phosphocreatine, 10 HEPES, 0.5 EGTA, 4 ATP-TRIS, 0.4 GTP-TRIS, 0.3% biocytin, 2 QX-314 (pH 7.2–7.3; 280–290 mOsm/L). These recordings were performed to analyze the excitatory drive received by PV+ and SST+ cells. Series

resistance in voltage-clamp were monitored throughout the experiment and cells that had substantial changes in series resistance (>15%) during recording were discarded. Recordings of spontaneous and miniature excitatory postsynaptic currents (sEPSC, mEPSCs) were performed in voltage-clamp at –70 mV in the presence of gabazine (1μM; Tocris Bioscience) and CGP55845 (2μM; Abcam Biochemicals) for sEPSCs and with addition of tetrodotoxin for mEPSCs (TTX; 1μM; Alomone Labs). Recordings of spontaneous and miniature inhibitory postsynaptic currents (sIPSC, mIPSCs) were performed in voltage-clamp at +10mV in the presence of NBQX (10μM; Abcam Biochemicals) and DL-AP5 (100μM; Abcam Biochemicals) for sISPCs and with addition of TTX (1μM) for mIPSCs. For recordings of thalamocortical electrically evoked AMPA/NMDA EPSC in layer IV PV+ cells, current pulses were delivered to the thalamic radiation (TR) via a tungsten concentric bipolar microelectrode placed in the white matter midway between the MGN and the AI (rostral to the hippocampus). Evoked AMPA (eAMPA) currents were recorded at -70 mV in presence of CGP (2μM) and gabazine (1μM), while evoked NMDA (eNMDA) currents were recorded at +40 mV in presence of NBQX (10μM) and confirmed after with the application of DL-AP5 (100μM).

Current-clamp recordings were obtained in ACSF containing synaptic blockers gabazine (1μM), CGP55845 (2μM) and kynurenic acid (2mM). For these recordings, we used an intracellular K+-based solution containing (in mM): 130 KMeSO4, 2 MgCl2, 10 di-Na-phosphocreatine, 10 HEPES, 4 ATP-Tris, 0.4 GTP-Tris, and 0.3% biocytin (Sigma), pH 7.2–7.3, 280–290 mOsm/L. Passive and active membrane properties were analyzed in current clamp mode: active membrane properties were recorded by subjecting cells to multiple current step injections (step size 40 pA) of varying amplitudes (–200 to 600 pA). In subsequent experiments, the same protocol was repeated in presence of the voltage gated potassium channel (Kv) blocker α-DTX (100nM; Alomone labs). In these experiments, slices were recovered in a holding chamber for at least 1 hr in presence of α-DTX. Once placed in recording chamber slices were kept for recording for max 1 hr. Passive

membrane properties, resting membrane potential (Vm), input resistance (Rin), and membrane capacitance (Cm) were obtained immediately after membrane rupture. Membrane potentials were maintained at –80 mV, series resistances (10–18 MΩ) and Rin were monitored on-line with a 40 pA current injection (150ms) given before each 500ms current injection stimulus. Only cells with resting membrane potential more negative than -60mV at the start of recording and spikes with overshoot were considered for further analysis. Data acquisition (filtered at 2–3 kHz and digitized at 10kHz; Digidata 1440, Molecular Devices, CA, United States) was performed using the Multiclamp 700B amplifier and the Clampex 10.6 software (Molecular Devices).

Electrophysiological data analysis

All analysis was performed by researchers blinds to the genotype. Analysis of electrophysiological recordings was performed using Clampfit 10.7 (Molecular Devices). For the analysis of sEPSCs, mEPSCs, sIPSCs and mIPSCs a minimum of 100 events were sampled per cell over a 2min period using an automated template search algorithm in Clampfit. The 20–80% rise time of the response and the decay time constant determined from the exponential fit (100–37%) were calculated. Charge transfer was calculated by integrating the area under the EPSC and IPSC waveforms. The mean PSC synaptic current was calculated as the charge transfer of the averaged PSC (ΔQ) multiplied by mean PSC frequency. For thalamocortical eAMPA and eNMDA, the mean amplitude of EPSCs including both failure and success was obtained from a total of 5 to 10 sweeps. Onset latency indicated the time from beginning of stimulus artifact and the onset of eAMPA or eNMDA. To measure eNMDA/eAMPA ratios, the eAMPA component was taken at the peak of EPSC at −70 mV, whereas the eNMDA component was measured at the peak of EPSC at +40 mV.

For the analysis of current-clamp recordings from PV cells, rheobase was measured as the minimal current necessary to evoke an action potential (AP). For the analysis of the AP properties, the first AP appearing within a 50ms time window from beginning of current pulse was analyzed. AP latency was measured as the time between current step onset and when membrane voltage reached

AP threshold. The AP amplitude was measured from the AP threshold to the peak. The AP half-width was measured at the voltage level of the half of AP amplitude. The AP rise and fall time were measured between the AP threshold and the maximal AP amplitude, and between the maximal AP amplitude and the AP end, respectively. The fast afterhyperpolarization (fAHP) amplitude was determined as the minimum voltage following the AP peak subtracted from the AP threshold. fAHP time was determined as the time between AP threshold and the negative peak of fAHP. The hyperpolarization-activated cation current (I_h)-associated voltage rectification (I_h sag) was determined as the amplitude of the membrane potential sag from the peak hyperpolarized level to the level at the end of the hyperpolarizing step when the cell was hyperpolarized to –100mV. Membrane time constant (τ) was calculated by the product of R_{in} and C_m. For the firing analysis, we considered only APs with amplitude >30 mV as full APs. Spikelets with amplitude smaller than 30mV were not analyzed in this study. The inter-spike interval (ISI) was determined by the time difference between adjacent AP peaks. Spike amplitude accommodation ratio (AAR) was calculated by dividing the amplitude of the last AP by the amplitude of the first generated in response to 2x rheobase current injection. Firing frequency adaptation ratios (FFAR) were calculated by dividing the last ISI with the first one of the responses to 2x rheobase current injection. The maximal (initial) firing frequency (F_{max}) was computed as the reciprocal of the average of the first 2 ISIs in a spike train elicited by the current step (max +600pA) applied before a noticeable appearance of spikelets. The steady-state firing frequency (F_{ss}) was computed as the reciprocal of the average of the last 4 ISIs in the spike train were Fmax was obtained. Finally, the # APs-current relationship for evoked firing was determined by injecting 500-ms somatic current steps of increasing amplitude (40pA increments) to a maximum of 600pA. For current-clamp recordings in presence of α-DTX experiments the delta (Δ) values were calculated for rheobase, AP threshold and AP number at +200pA, by subtracting individual values of α-DTX-treated cells from the average of their respective control group.

Hierarchical clustering and principal component analysis (PCA)

This analysis was based on previous published data finding heterogeneity in PV+ interneurons population (Helm et al., 2013), and performed using the software IBM SPSS V29.0.0. Hierarchical clustering was based on Euclidean distance of PV+ cells from control mice. To identify potential clusters, we used AP-Half width and Max frequency values. We then performed multidimensional cluster analysis on passive and active membrane properties to identify possible common groupings of PV+ interneurons using the software Prism 9.0 (GraphPad Software). In our database, we focused on 13 parameters (see ***Figure 6b***) that were for the majority unrelated. ***Figure 6*** is a cross-correlation matrix of these 13 parameters with correlation indices shade coded, with black being perfectly correlated (correlation index of 1.0) and white being perfectly uncorrelated (correlation index of 0). We therefore performed PCA on the 13 parameters to reduce the dimensionality and to potentiate clusters separation.

Immunohistochemistry, cell reconstruction and anatomical identification

For post-hoc anatomical identification, every recorded neuron was filled with biocytin (0.5%, Sigma) during whole-cell recordings (15 min). To reveal biocytin, the slices were permeabilized with 0.3% triton X-100 and incubated at 4 °C with a streptavidin-conjugated Alexa-488 (1:1000) in TBS. For PV and SST immunofluorescence, sections were permeabilized with 0.25.1–0.3% Triton X-100 in PBS and incubated in blocking solution containing 120% normal goat serum (NGS) for 1 h. Then, sections were incubated with the following primary antibodies diluted in 1% NGS, 0.25% Triton-X 100 in PBS: were incubated with primary antibodies mouse anti-PV (1:1000, Swant, Cat# 235) and rabbit anti-SST (1:500, Thermofisher Invitrogen, Cat# PA5-82678) at 4°C for 48-72 h. , Sections were then washed in PBS (3X- 10 mins each), incubated for 2 hrs at RT with the following secondary antibodies diluted in 1% NGS, 0.25% Triton-X 100 in PBS and mounted on microscope slides: streptavidin conjugated Alexa 488 followed by incubation with conjugated secondary antibodies for 4h at RT, rinsed, and mounted on microscope slides. The secondary antibodies used

were Alexa-Fluor conjugated 488 (1:1000, Invitrogen, Cat# S11223), Alexa 555-conjugated goat anti-rabbit (1:500; Life technologies, A21430) and Alexa 555 (1:500) and 647-conjugated goat anti-mouse (1:250, Cell signaling, 4410S). Z-stacks of biocytin-filled cells were acquired with a 1µm step using a 20x objective (NA 0.75) on the Leica SP8-DLS confocal microscope. Confocal stacks were merged for detailed reconstruction in Neuromantic tracing software version 1.7.5 (Myatt et al., 2012). Dendritic arbors were reconstructed plane-by-plane from the image z-stack and analyzed using the Neuromantic software. Sholl analysis of reconstructed dendritic arbors was performed in FIJI software using the plugin Neuroanatomy. This analysis was performed in radial coordinates, using a 10µm step size from r=0, with the origin centered on the cell soma, and counting the number of compartments crossing a given radius. All analysis was performed by researchers blinds to the genotype.

vGlut1/PSD95 and vGlut 2/PSD immunostaining, imaging and quantification

P60 mice were anesthetized with: Ketamine-100mg/kg+Xylazine-10mg/kg+Acepromazine-10mg/kg and perfused transcardially with 0.9% saline followed by 4% Paraformaldehyde (PFA) in phosphate buffer (0.1M PB, pH 7.2-7.4). Brains were dissected out and post-fixed in 4% PFA overnight at 4°C. They were subsequently transferred to 30% sucrose (prepared in PBS, pH 7.2) at 4°C for 48 hrs. Brains were then embedded in molds filled with OCT Tissue Tek and frozen in a bath of 2-methybutane placed on a bed of dry ice and ethanol. Coronal sections were cut at 40µm with a cryostat (Leica CM3050 S) and collected as floating sections in PBS. Brain sections were first permeabilized in 0.2 % Triton-X in PBS for 1 hr at RT and then blocked in 10% normal donkey serum (NDS) with 0.2% Triton-X 100 and 5% bovine serum albumin (BSA) in PBS for 2 hrs at RT followed by incubation at 4°C for 48 hrs with the following primary antibodies diluted in 5% NDS, 0.2% Triton-X 100 and 2 % BSA in PBS: goat anti-PV (1:1000, Swant, Cat# PVG-213), rabbit anti-VGlut1 (1:100 Thermo Fisher/ Invitrogen, Cat# 48-2400), rabbit anti-VGlut2 1:1000, Synaptic systems, Cat# 135402) mouse anti-PSD95 (1:500, Invitrogen, Cat# MA1-05). Sections were then

washed in PBS + 0.1% Triton-X 100 (3X10 mins each) and incubated for 2 hrs at RT with the following secondary antibodies diluted in 5% NDS, 0.2% Triton-X 100 and 2 % BSA in PBS : Alexa 488-conjugated donkey anti-rabbit (1:500, Life technologies/ Invitrogen, Cat# A11055), Alexa 555-conjugated donkey anti-mouse (1:500, Life technologies/ Invitrogen, Cat# A31570), Alexa 633-conjugated donkey anti-goat (1:500, Invitrogen, Cat# A21082). Sections were rinsed in 0.1% Triton-X 100 in PBS (3X10' each +1X5') and mounted with Vectorshield mounting medium (Vector).

Confocal Imaging and quantification: Immunostained sections were imaged using a Leica SP8-STED confocal microscope, with a 63x (NA 1.4) at 1024 X 1024, zoom=1, z-step =0.3 µm, stack size of ~15 µm. Images were acquired from the auditory cortex from at least 3 coronal sections per animal. Acquisition and analysis of images were done by an experimenter blind to the genotype. Perisomatic puncta density was analysed using Image J-Fiji. At least 5 cells were chosen from each slice and puncta was quantified by drawing an ROI around each PV-positive cell soma. All images were post-processed for analysis using an appropriate filter, thresholded, and puncta was counted using the Analyze particles macro in ImageJ/Fiji. All analysis was performed by researchers blinds to the genotype. No mouse was excluded from this analysis.

Statistics

Data were expressed as mean±SEM. For statistical analysis, we based our conclusion on the statistical results generated by linear mixed model (LMM), modelling animal as a random effect and genotype as fixed effect. We used this statistical analysis because we considered the number of mice as independent replicates and the number of cells in each mouse as repeated measures. For comparison with LMM analysis, we also tested the data for normality with a Shapiro–Wilcoxon test, then if data were normally distributed, standard parametric statistics were used (unpaired t-test), while if data were not normally distributed, non-parametric Mann–Whitney test was used for comparisons of two groups. The two statistical analyses were always performed for all the data of

the study and indicated in the tables related to each figure. Two-way ANOVA with Sidak's multiple comparison post hoc test was used for the detection of differences in AP firing and number of dendritic intersections between genotypes. Statistical analysis was performed using Sigma Plot 11.0, Prism 9.0 (GraphPad Software) and IBM SPSS V29.0.0 for LMM analysis.

Figures

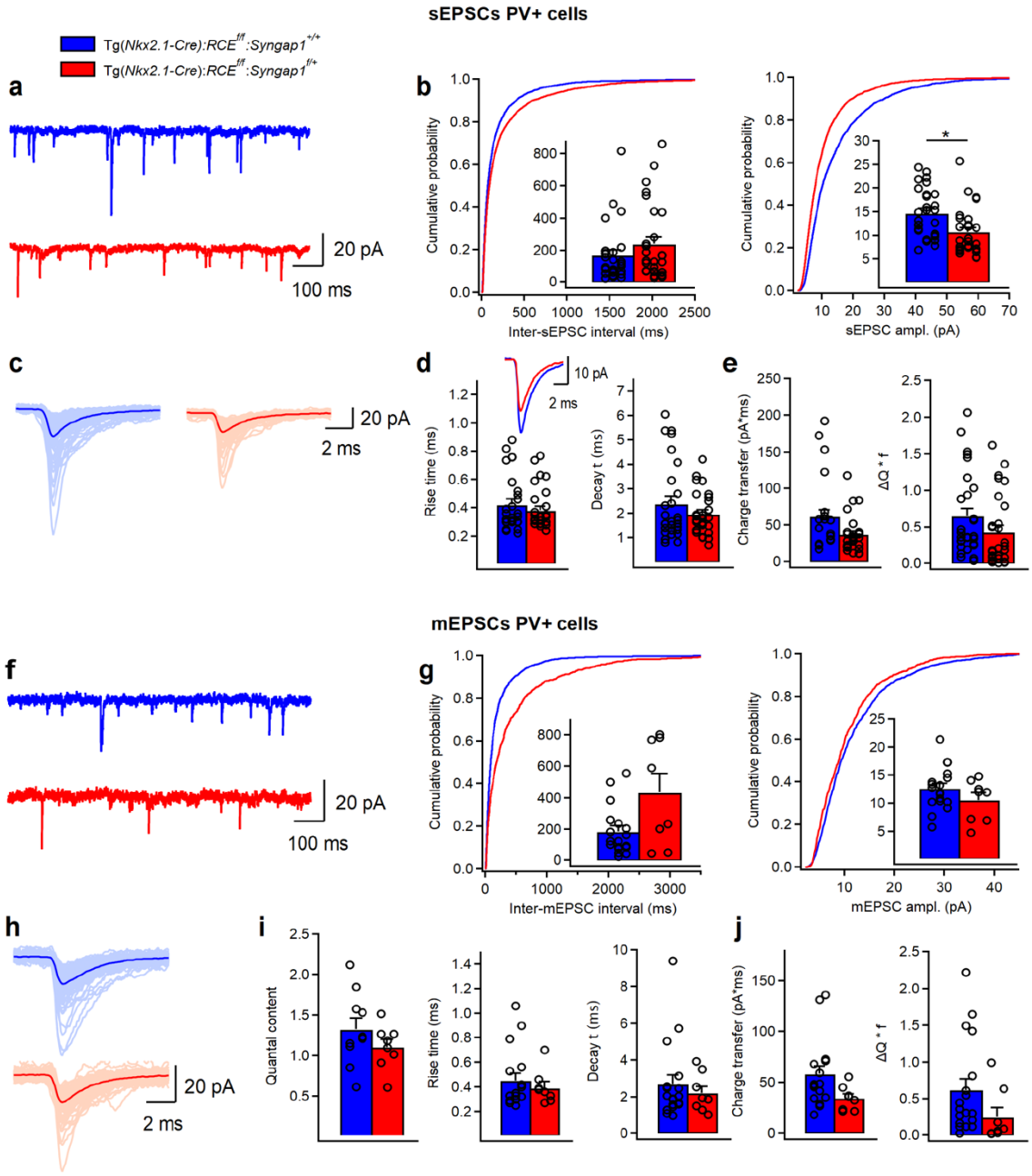

Figure 1. *Syngap1* haploinsufficiency in Nkx2.1+ interneurons is associated with reduced sEPSC amplitude and mEPSC frequency in LIV PV+ cells. (**a**) Representative traces of sEPSCs recorded in PV+ cells from control Tg(*Nkx2.1-Cre*)*:RCE$^{f/f}$:Syngap1$^{+/+}$* (blue, n=28 cells, 11 mice) and cHet Tg(*Nkx2.1-Cre*)*:RCE$^{f/f}$:Syngap$^{f/+}$* (red, n=28 cells, 11 mice) mice. (**b**) , Cumulative

probability plots show a significant decrease in the amplitude (p=0.048, LMM) and no change in the inter-sEPSC interval (LMM, p=0.186). Insets illustrate significant differences in the sEPSC amplitude for inter-cell mean comparison (*p=0.044, LMM) and no difference for inter-sEPSC interval (p=0.676, LMM). (**c**) Representative examples of individual sEPSC events (100 pale sweeps) and average traces (bold trace) detected in PV cells of control and cHet mice. (**d**) Superimposed scaled traces (left top) and summary bar graphs for a group of cells (bottom) show no significant differences in the sEPSCs kinetics (p=0.350, LMM for rise time, and p=0.429, LMM for decay time). (**e**) Summary bar graphs showing no differences for inter-cell mean charge transfer (p=0.064, LMM, left) and for the charge transfer when frequency of events is considered (p=0.220, LMM). (**f**) Representative traces of mEPSCs recorded in PV+ cells from control (blue, n=18 cells, 7 mice) and cHet (red, n=8 cells, 4 mice) mice. (**g**) Cumulative probability plots show no change in the amplitude of mEPSC (p=0.135, LMM) and an increase in the inter-mEPSC interval (*p=0.027, LMM). Insets illustrate summary data showing no significant differences in the amplitude (p=0.185, LMM) and the inter-mEPSCs interval for inter-cell mean comparison (p=0.354, LMM). (**h**) Representative examples of individual mEPSC events (100 pale sweeps) and average traces (bold trace) detected in PV+ cells of control and cHet mice. (**i**) Summary bar graphs for a group of cells show no significant differences in the quantal content (p=0.222, LMM) and mEPSCs kinetics (p=0.556, LMM for rise time, and p=0.591, LMM for decay time). (**j**) Summary bar graphs showing no differences for inter-cell mean charge transfer (p=0.069, LMM, left) and for the charge transfer when frequency of events is considered (p=0.137, LMM).

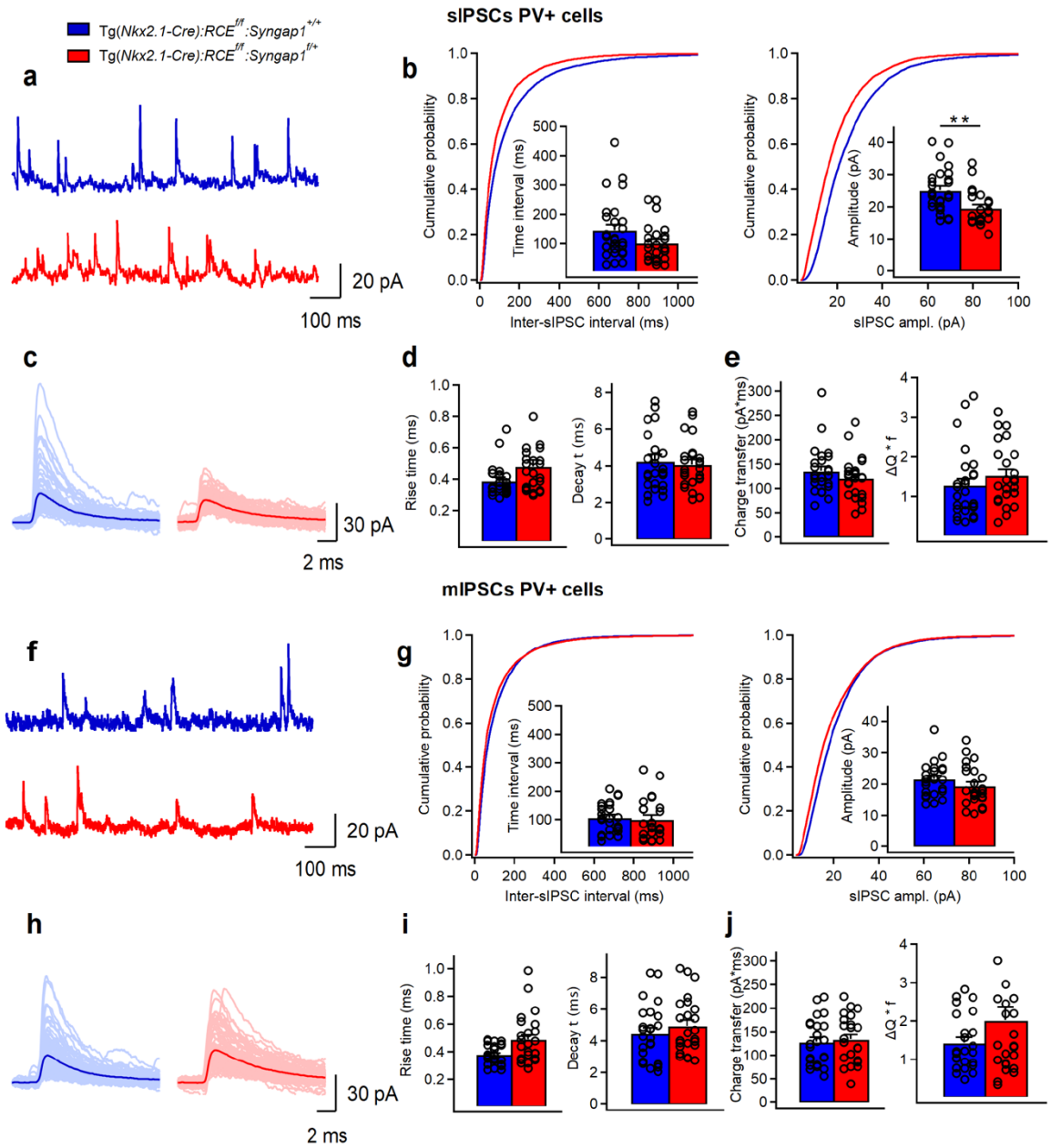

Figure 2. The amplitude of sIPSCs, but not mIPSCs, in LIV PV+ cells is reduced in Tg(*Nkx2.1-Cre*):*RCE*$^{f/f}$:*Syngap1*$^{f/+}$ mice (**a**) Representative traces of sIPSCs recorded in PV+ cells from control (blue, n=27 cells, 8 mice) and cHet (red, n=24 cells, 7 mice) mice. (**b**) , Cumulative probability plots show a significant decrease in the amplitude (**p=0.003, LMM) and no change in the inter-sIPSC interval (LMM, p=0.069). Insets illustrate significant differences in the sIPSC amplitude for inter-cell mean comparison (**p=0.002, LMM) and no difference for inter-sIPSC interval (p=0.102, LMM). (**c**) Representative examples of individual sIPSC events (100 pale

sweeps) and average traces (bold trace) detected in PV cells of control and cHet mice. (**d**) Summary bar graphs for a group of cells show no significant differences in the sIPSCs kinetics (p=0.113, LMM for rise time, and p=0.602, LMM for decay time). (**e**) Summary bar graphs showing no differences for inter-cell mean charge transfer (p=0.234, LMM, left) and for the charge transfer when frequency of events is considered (p=0.273, LMM). (**f**) Representative traces of mIPSCs recorded in PV+ cells from control (blue, n=25 cells, 8 mice) and cHet (red, n=24 cells, 7 mice) mice. (**g**) Cumulative probability plots show no change in the amplitude of mIPSC (p=0.118, LMM) and in the inter-mIPSC interval (p=411, LMM). Insets illustrate summary data showing no significant differences in the amplitude (p=0.195, LMM) and the inter-mIPSCs interval for inter-cell mean comparison (p=0.243, LMM). (**h**) Representative examples of individual mIPSC events (100 pale sweeps) and average traces (bold trace) detected in PV+ cells of control and cHet mice. (**i**) Summary bar graphs for a group of cells show no significant differences in the mIPSCs kinetics (p=0.103, LMM for rise time, and p=0.597, LMM for decay time). (**j**) Summary bar graphs showing no differences for inter-cell mean charge transfer (p=0.374, LMM, left) and for the charge transfer when frequency of events is considered (p=0.100, LMM).

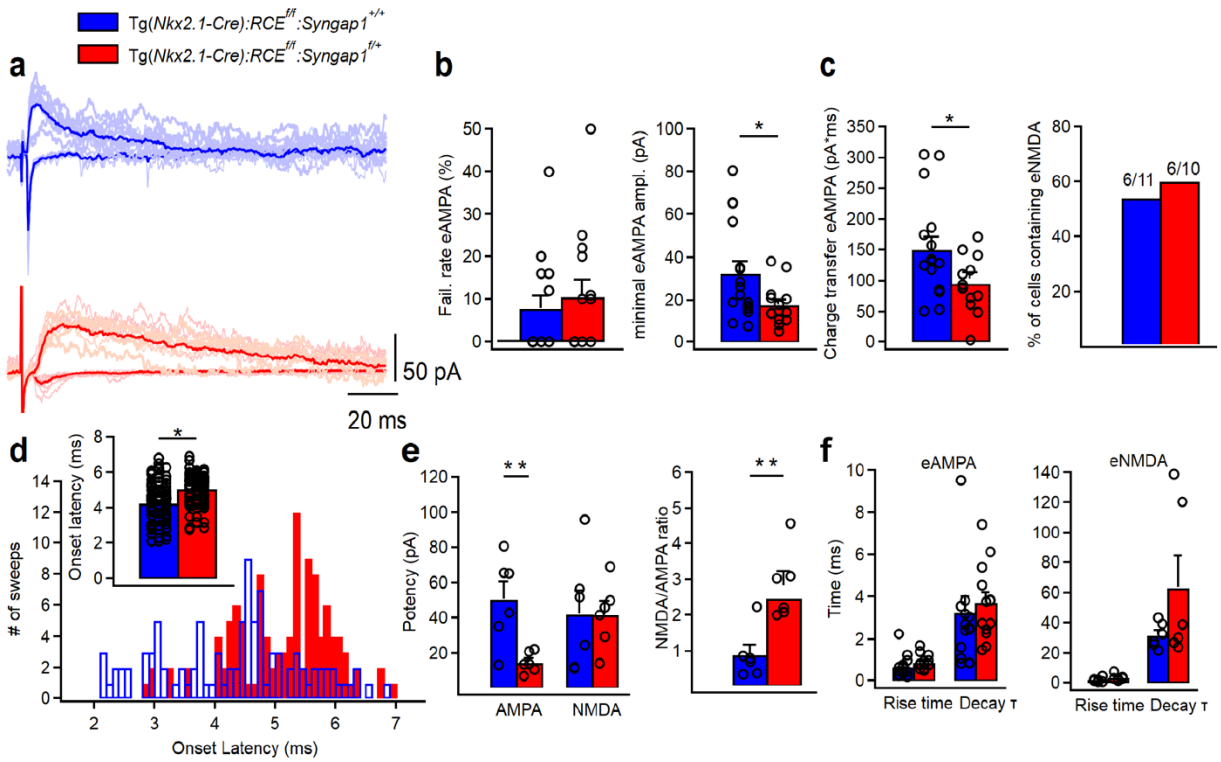

Figure 3. Thalamocortical eAMPA transmission is decreased in LIV PV+ cells from Tg(*Nkx2.1-Cre*):*RCE*$^{f/f}$:*Syngap1*$^{f/+}$ mice. (**a**) Representative examples of individual eAMPA (negative deflections) and eNMDA (positive deflections) (5-10 pale sweep) and average traces (bold trace) recorded in PV cells from control (blue, n=16 cells, 7 mice) and cHet mice (red, n=14 cells, 7 mice). (**b**) Summary plots showing no change in the failure rate of eAMPA (left, p=0.550, LMM) and a significant increase in the minimal (including failures and successes) eAMPA amplitude (*p=0.031, LMM) and (**c**, left) charge transfer (*p=0.033, LMM) in cHet mice. (**c**, right) Summary bar graph illustrating the percentage of PV+ cells containing eNMDA in the thalamocortical evoked EPSC. (**d**) Synaptic latency histograms (bottom) of thalamocortical eEPSC from control and cHet mice, and summary bar graph (top) illustrating an increase in the onset latencies of eEPSC in cHet mice (*p=0.023, LMM). For both histograms, bins are 0.1 msec wide. (**e**) Summary plots showing a significant increase in the potency of eAMPA (successes only, **p=0.003, LMM, left) in cHet mice with no change in eNMDA (p=0.969, LMM), A significant

increase is present in the NMDA/AMPA ratio (i.e. ratio of the peak for eNMDA and eAMPA, **p=0.001, LMM, right) in cHet mice. (**f**) Summary plots showing no significant differences in the eAMPA (p=0.177, LMM for rise time, and p=0.608, LMM for decay time) and eNMDA kinetics (p=0.228, LMM for rise time, and p=0.221, LMM for decay time).

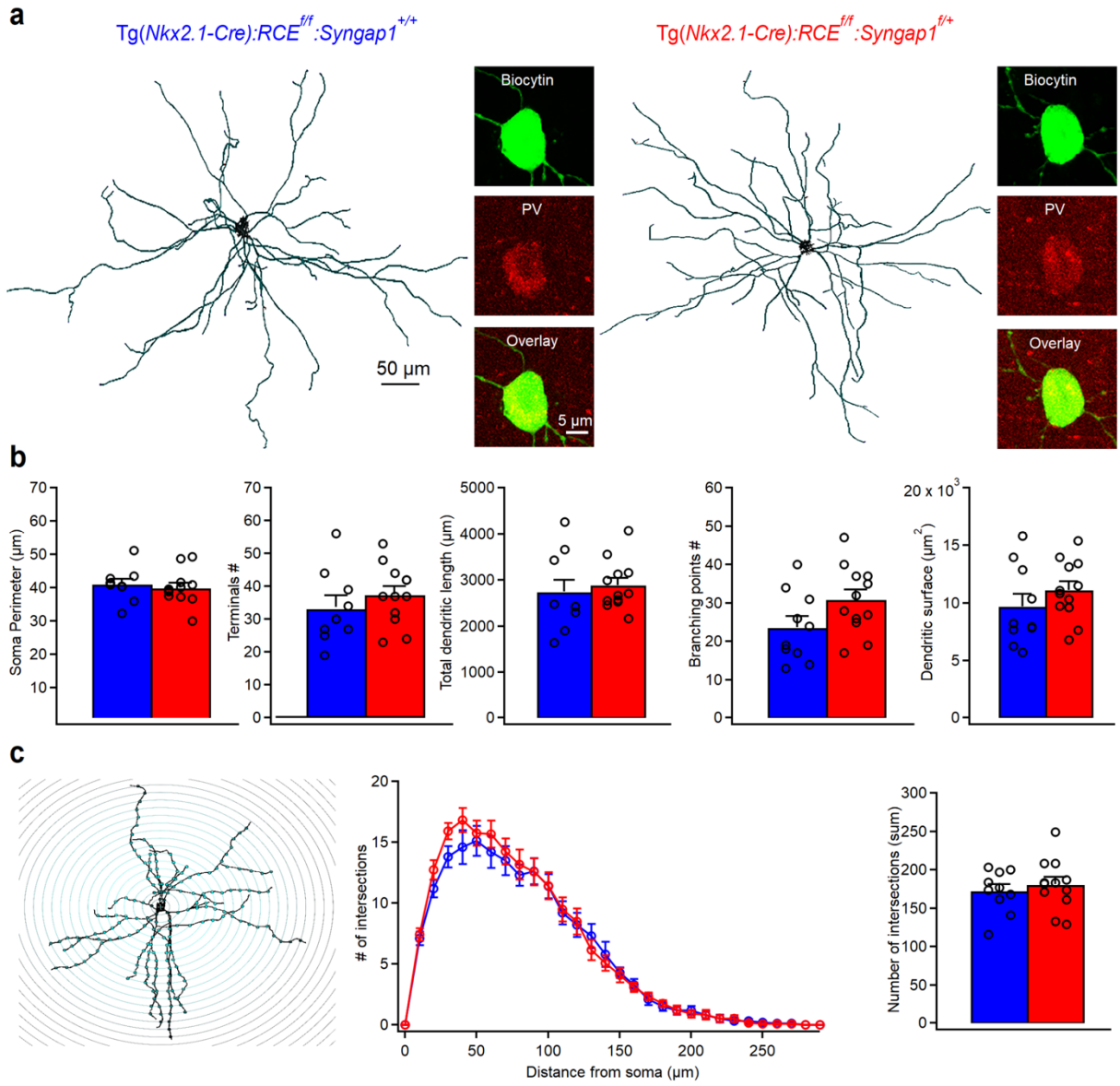

Figure 4. *Syngap1* haploinsufficiency in Nkx2.1+ interneurons does not appear to alter the dendritic arbour of PV+ cells. (**a**) Anatomical reconstructions of PV+ cells filled with biocytin in control (left, n=10 cells, 6 mice) and cHet (right, n=12 cells, 7 mice) during whole-cell patch-clamp recordings and post hoc immunohistochemical validation of BC interneurons confirming the positivity for PV. (**b**) Summary data showing no differences in somatic (p=0.636, LMM) and dendritic parameters between the two genotypes (p=0.456 for terminals #, p=0.887 for total

dendritic length, p=0.100 for branching points # and p=0.460 for dendritic surface area, LMM). (c, left) Representative reconstruction of PV+ cells and superimposed concentric circles used for Sholl analysis, with a radius interval of 10 µm from the soma. (**c**, center) Sholl analysis of PV+ cells dendritic branch patterns revealed no differences in the number of dendritic intersections (Two-way Repeated Measure ANOVA with Sidak's multiple comparison post hoc test, p=0.937). (**c**, right) Summary bar graph showing no differences in the total number of dendritic intersections obtained from Sholl analysis in control and cHet mice (p=0.502, LMM).

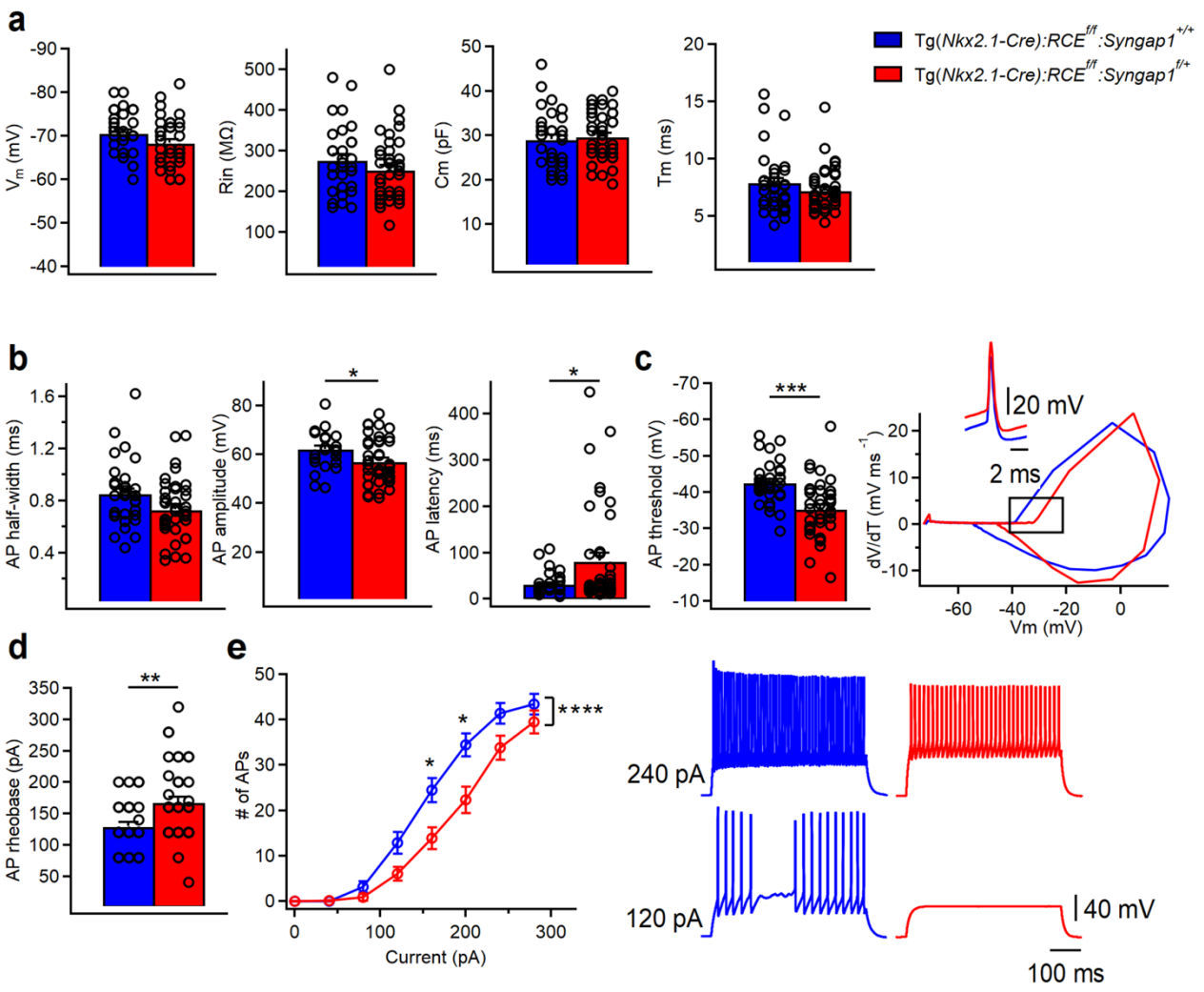

Figure 5. PV+ cells intrinsic excitability is decreased in Tg(*Nkx2.1-Cre*):*RCE*$^{f/f}$:*Syngap1*$^{f/+}$ mice. (**a**) Summary data showing no changes in the passive membrane properties between control (blue, n=33 cells, 15 mice) and cHet mice (red, n=40 cells, 17 mice) (p=0.081 for Vm, p=0.188 for Rin, p=0.188 for Cm, p=0.199 for Tm, LMM) (**b**) Summary data showing no differences in AP half-width (p=0.111, LMM) but a significant decrease in AP amplitude (*p=0.032, LMM) and a significant increase in AP latency (*p=0.009, LMM) from PV+ cells recorded in cHet mice. (**c**, left) Summary bar graph shows a significant decrease in AP threshold from cHet mice (***p<0.001, LMM) and phase plane (Vm versus dV/dt, **c**, right bottom) for the first AP generated confirmed this result with a more hyperpolarized value (the area squared) of AP threshold for generation of AP. (**c**,

right top) Representative single APs evoked by rheobase currents from control and cHet mice. Action potentials are aligned at 50% of the rising phase on X axis and peak on Y axis. Note the more hyperpolarized AP with consequent reduction in AP amplitude in PV+ cells from cHet mice. (**d**) Summary bar graph shows a significant increase in the rheobase current (**p=0.004, LMM). (**e**, left) Summary plot showing a reduction of averaging number of APs per current step (40 pA) amplitude recorded from LIV PV+ cHet (red circles, n=38 cells; 18 mice) compared to control (blue circles, n=30 cells, 15 mice) neurons, including group averages (± S.E.M., Two-way Repeated Measure ANOVA with Sidak's multiple comparison post hoc test, ****p<0.0001). (**e**, right) Representative voltage responses indicating the typical FS firing pattern of PV+ cells in control and cHet mice in response to depolarizing (+120 pA and +240 pA) current injections corresponding to rheobase and 2x rheobase current.

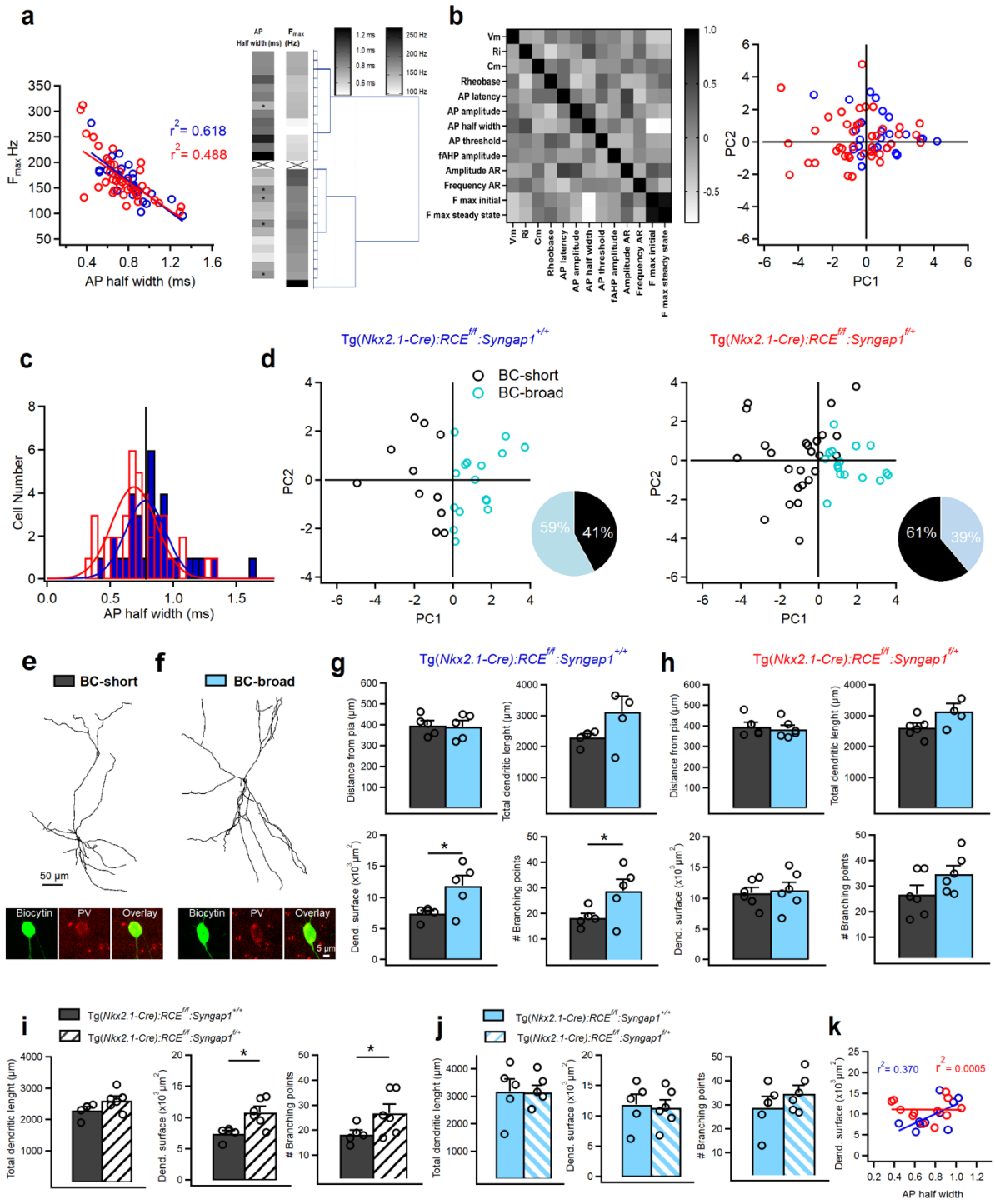

Figure 6. *Syngap1* haploinsufficiency in Nkx2.1+ interneurons affects the denritic arbour of a specific subpopulation of LIV PV+ cells. (**a**, left) Strong negative correlation of F_{max} with AP half-width in PV+ cells from control (blue, n=33 cells, 15 mice) and cHet mice (red, n=40 cells, 17 mice). (**a**, right) Hierarchical clustering based on Euclidean distance of PV+ cells from control

mice. Clustering is based on AP-Half width and Max frequency. Asterisks indicate cells with longer AP-half width felling into the cluster including PV+ cells with higher of values of Fmax. (**b**, left) Correlation of parameters describing membrane properties of PV+ interneurons. The 13 passive and active membrane properties used for PCA analysis (derived from 27 PV+ cells from control mice; see materials and methods) are arrayed against each other in a correlation matrix with the degree of correlation indicated by the shading: white is uncorrelated (correlation index of 0) and black is perfectly correlated (correlation index of 1, diagonal squares). PCA on the 13 parameters to reduce the dimensionality. (**b**, right) The first (PC1) and second (PC2) PC values derived for each interneuron are plotted against each other. No clear separation of subgroups in scatterplot of first 2 PCs is present when genotype is taken into consideration. (**c**) Cumulative histograms of AP half widths in control (n=33 cells, 15 mice) and cHet mice (n=40 cells, 17 mice) fitted with two Gaussian curves. Vertical line indicates the cutoff value at intersection between the two curves. For both histograms, bins are 0.05 msec wide. (**d**) PCA analysis using the cutoff value of 0.78 ms and the 13 passive and active membrane properties distinguish two subgroups of PV+ cells with short (black circles) and broad (turquoise circles) AP-half width duration in both genotypes. Insets illustrate pie charts describing the % of two subgroups of PV+ cells in the control and cHet mice. (**e**) Anatomical reconstructions of a BC-short and (**f**) a BC-broad filled with biocytin in control mice during whole-cell patch-clamp recordings and post hoc immunohistochemical validation for PV. (**g**) Summary data in control mice (gray, BC-short n=5 cells, 4 mice; turquoise, BC-broad n=5 cells, 4 mice) showing no significant difference in terms of distance from pia (p=0.856, LMM) for both subtypes of PV+ cell analyzed indicating LIV location and significant differences in dendritic parameters between the two subpopulations of PV+ cells (*p= 0.016 for dendr. surface area, *p=0.043 for # branching points, LMM) and no change in total dendritic length (p=0.057, LMM). (**h**) Summary data in cHet mice (gray, BC-short n=6 cells, 4 mice; turquoise, BC-broad n=6 cells, 3 mice) showing no significant difference in terms of distance from pia (p=0.594, LMM) for both subtypes of PV+ cell and all dendritic parameters (p= 0.062 for total dendritic length, p=0.731 for

dendr. surface area, p=0.081 for # branching points, LMM). (**i**) Summary data showing a significant increase in dendritic complexity between control (gray, n=5 cells, 4 mice) and cHet (white, n=6 cells, 4 mice) for the subpopulation of BC-short (*p=0.009 for dendr. surface area, *p=0.048 for # branching points, LMM) and no difference for the total dendritic length (p=0.070, LMM). (**j**) Summary data showing preserved dendritic parameters in cHet (turquoise filled with pattern, n=6 cells, 3 mice) Vs control (turquoise, n=5 cells, 4 mice) (p= 0.967 for total dendritic length, p=0.784 for dendr. surface area, p=0.290 for # branching points, LMM). (**k**) The strong positive correlation of dendritic surface area with AP half-width is present only in PV+ cells from control mice (blue, n=10 cells, 8 mice) and disappears in cHet mice (red, 12 cells, 7 mice).

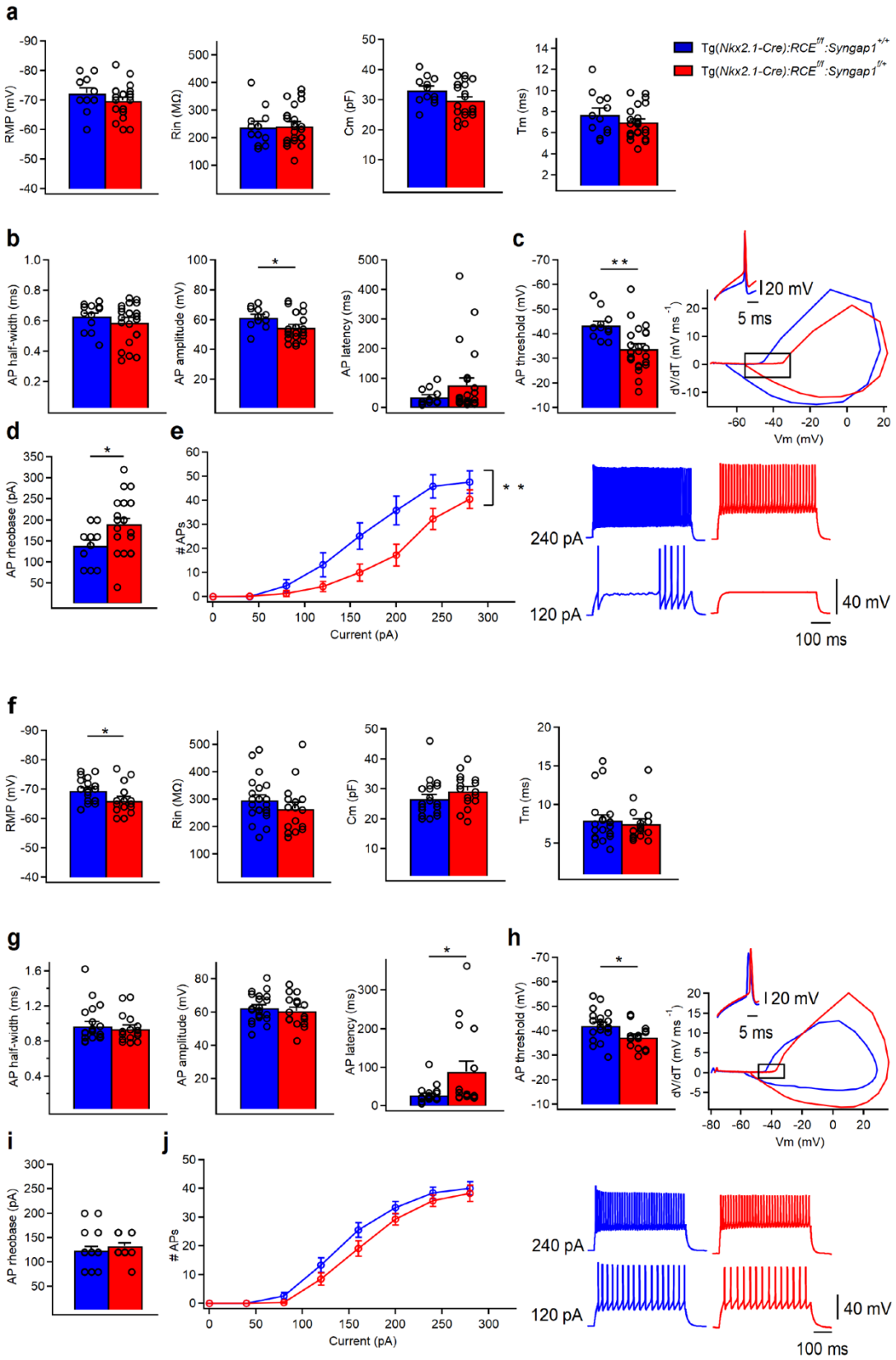

Figure 7. Intrinsic excitability is decreased in both subpopulations of PV+ cells in cHet mice

(**a**) Summary data showing no changes in the passive membrane properties of BC-short between

control (blue, n=12 cells, 9 mice) and cHet mice (red, n=24 cells, 13 mice) (p=0.189 for Vm, p=0.856 for Rin, p=0.188 for Cm, p=0.077 for Tm, LMM) (**b**) Summary data showing no differences in AP half-width (p=0.386, LMM) and AP latency (p=0.210, LMM) but a significant decrease in AP amplitude (*p=0.024, LMM) of BC-short recorded in cHet mice. (**c**, left) Summary bar graph shows a significant decrease in AP threshold from cHet mice (**p=0.002, LMM) and phase plane (c, center) for the first AP generated confirmed this result with a more hyperpolarized value (the area squared) of AP threshold for generation of AP. (**c**, right) Representative single APs evoked by rheobase currents from control and cHet mice. (**d**) Summary bar graph shows a significant increase in the rheobase current (*p=0.015, LMM). (**e**, left) Summary plot showing a reduction of averaging number of APs per current step (40 pA) amplitude recorded from LIV BC-short in cHet (red circles, n = 22 cells; 13 mice) compared to control (blue circles, n = 11 cells, 9 mice) neurons, including group averages (± S.E.M., Two-way Repeated Measure ANOVA with Sidak's multiple comparison post hoc test, **p=0.005). (**e**, right) Representative voltage responses indicating the typical FS firing pattern of BC-short in control and cHet mice in response to depolarizing (+120 pA and +240 pA) current injections corresponding to rheobase and 2x rheobase current. (**f**) Summary data showing a significant decrease in RMP (*p=0.023, LMM) of BC-broad from cHet mice (red, n=16 cells, 11 mice) but no changes in the other passive membrane properties compared to control mice (blue, n=21 cells, 12 mice) (p=0.244 for Rin, p=0.170 for Cm, p=0.639 for Tm, LMM). (**g**) Summary data showing no differences in AP half-width (p=0.593, LMM) and AP amplitude (p=0.713) and a significant increase in AP latency (*p=0.035, LMM) from BC-broad cells recorded in cHet mice. (**h**, left) Summary bar graph shows a significant decrease in AP threshold from cHet mice (*p=0.010, LMM) and phase plane (**h**, center) for the first AP generated confirmed this result with a more hyperpolarized value (the area squared) of AP threshold for generation of AP. (**h**, right). Representative single APs evoked by rheobase currents from control and cHet mice. (**i**) Summary bar graph shows no difference in the rheobase current (p=0.402, LMM). (**j**, left) Summary plot showing no difference in the averaging number of APs per current

step (40 pA) amplitude recorded from LIV BC-broad in cHet (red circles, n=16 cells, 11 mice) compared to control (blue circles, n=18 cells; 11 mice) neurons, including group averages (± S.E.M., Two-way Repeated Measure ANOVA with Sidak's multiple comparison post hoc test, p= 0.333). (**j**, right) Representative voltage responses indicating the typical FS firing pattern of BC broad in control and cHet mice in response to depolarizing (+120 pA and +240 pA) current injections corresponding to rheobase and 2x rheobase current.

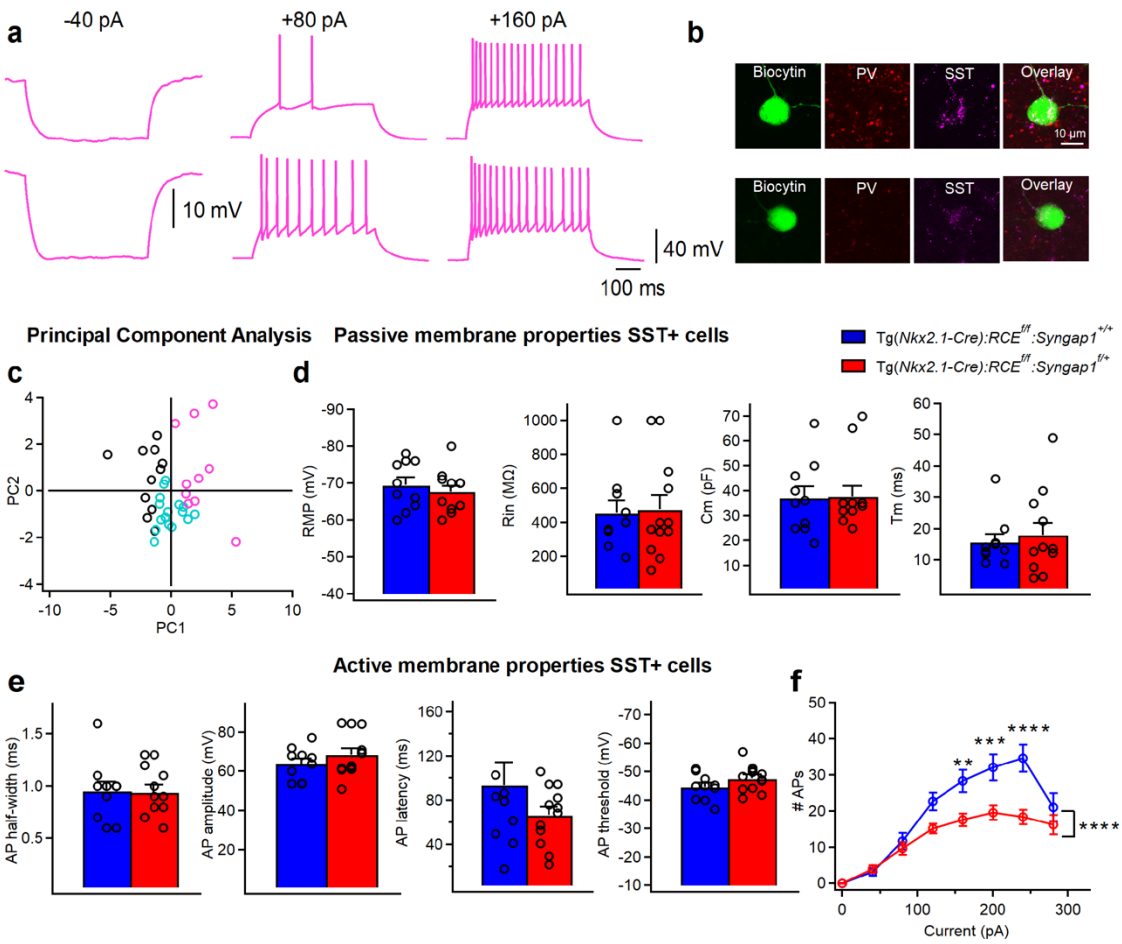

Figure 8. Intrinsic excitability of SST+ cells is less affected by embryonic-onset *Syngap1* haploinsufficiency in Nkx2.1 interneurons. (**a**) Representative voltage responses indicating the typical regular adapting firing pattern of SST+ in control mice in response to hyperpolarizing (-40 pA) and depolarizing (+80 pA and +160 pA) current injections corresponding to Ih associated voltage rectification, rheobase and 2x rheobase current respectively. (**b**) Post hoc immunohistochemical validation of these interneurons confirming their positivity for SST+ and negativity for PV-. (**c**) PCA using the 13 parameters previously described clearly separate the cluster of SST+ cells (pink circles) from BC-short (black circles) having however some overlaps with BC-broad (turquoise circles) in control mice. (**d**) Summary data showing no changes in the passive (p=0.469 for Vm, p=0.681 for Rin, p=0.922 for Cm, p=0.922 for Tm, LMM) and (**e**) active

membrane properties (p=0.675 for AP half width, p=0.342 for AP amplitude, p=0.081 for AP latency, p=0.119 for AP threshold, LMM) between SST+ cells from control (blue, n=10 cells, 7 mice) and cHet mice (red, n=12 cells, 7 mice) (**f**) Summary plot showing a reduction of averaging number of APs per current step (40 pA) amplitude recorded from LIV SST+ in cHet (red circles, n= 12 cells, 8 mice) compared to control (blue circles, n=8 cells, 7 mice) neurons, including group averages (± S.E.M., Two-way Repeated Measure ANOVA with Sidak's multiple comparison post hoc test, ****p<0.0001).

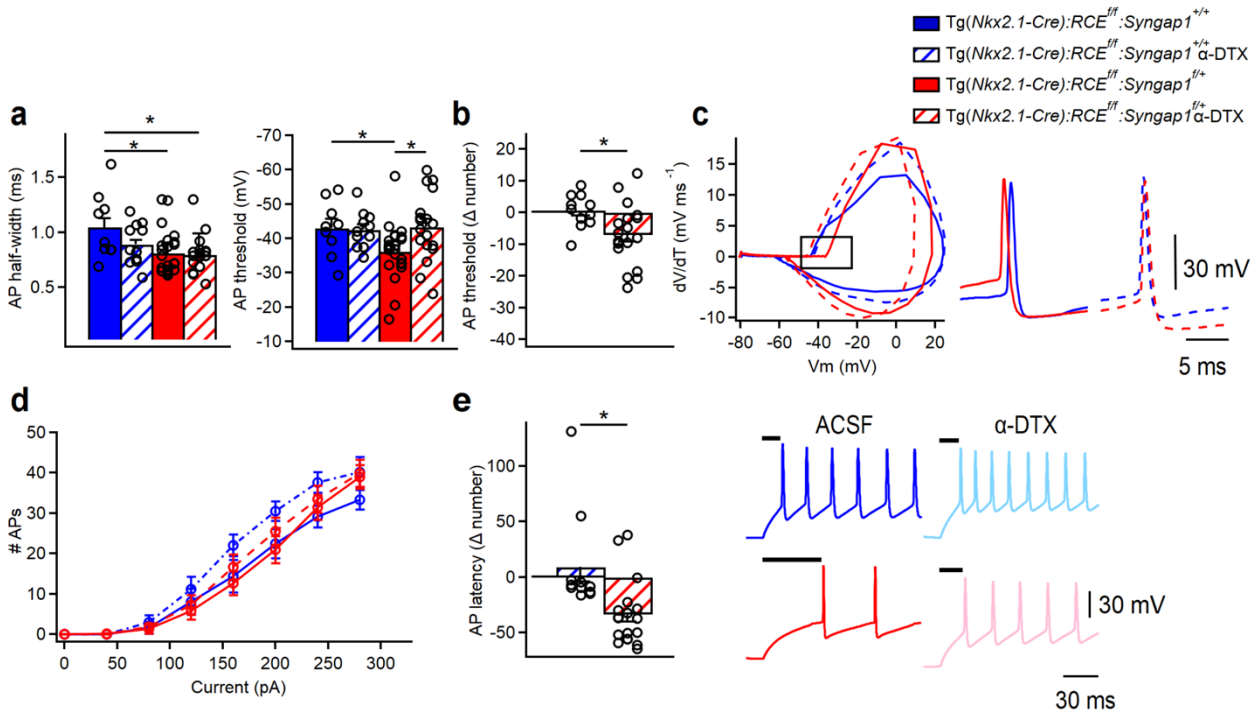

Figure 9. *Syngap1* haploinsufficiency alters the intrinsic excitability of LIV PV+ cells through Kv1 channels. (**a**, left) Summary bar graph shows a significant decrease in AP half-width from cHet mice in absence (*p=0.034, LMM) or presence of α-DTX (*p=0.039, LMM). (**a**, right) Summary bar graph shows a significant decrease in AP threshold of PV+ cells from cHet mice (*p=0.049, LMM) and the rescue of this deficit in presence of α-DTX (p=0.940, LMM). (**b**) delta (Δ) value was calculated for AP threshold by subtracting individual values of α-DTX-treated cells from the average of their respective control group. A significant increase in AP threshold Δ number was found for cHet treated PV+ cells (*p=0.015, LMM). (**c**. left) Phase plane for the first AP generated confirmed this result with more depolarized value (the area squared) of AP threshold in cHet treated cells (red dotted line). (**c**, center and right) Representative single APs evoked by rheobase currents from control and cHet mice (center), and control and cHet treated PV+ cells (blue and red dotted lines) . Of note the more hyperpolarized AP in cHet PV+ cells and the rescue of this deficit in presence of α-DTX. (**d**) Summary plot showing no difference in the averaging number of

APs per current step (40 pA) amplitude recorded from LIV PV+ in cHet treated and not treated PV+ cell compared to control neurons in presence or absence of α-DTX , including group averages (± S.E.M., Two-way Repeated Measure ANOVA with Sidak's multiple comparison post hoc test, p>0.05). (**e**, left) Summary bar graph shows a significant difference in AP latency Δ number (*p=0.006, LMM); (**e**, right) representative voltage traces clearly show a reduction in the AP onset for PV+ cells treated with α-DTX (pink trace). (Control, n=9 cells, 4 mice; control α-DTX-treated, n=11 cells, 6 mice; cHet, n=23 cells, 10 mice; cHet α-DTX-treated, n=18 cells, 8 mice).

References

Aceti M, Creson TK, Vaissiere T, Rojas C, Huang WC., Wang YX, Petralia RS, Page DT, Miller CA, Rumbaugh G (2015) Syngap1 Haploinsufficiency damages a postnatal critical period of pyramidal cell structural maturation linked to cortical circuit assembly. *Biological Psychiatry*, 77, 805–815. https://doi.org/10.1016/j.biopsych.2014.08.001

Aizenberg M, Mwilambwe-Tshilobo L, Briguglio JJ, Natan RG, Geffen, MN (2015) Bidirectional regulation of innate and learned behaviors that rely on frequency discrimination by cortical inhibitory neurons. *PLoS Biology*, 13, e1002308. https://doi.org/10.1371/JOURNAL.PBIO.1002308

Arora V, Michaelson S, Aceti M, Kilinic M, Miller C, Rumbaugh, G (2022) Syngap1 regulates cortical circuit assembly by controlling membrane excitability. *BioRxiv*. https://doi.org/10.1101/2022.12.06.519295

Bakken TE, Jorstad NL, Hu Q, Lake BB, Tian W, Kalmbach BE, Crow M, Hodge RD, Krienen FM, Sorensen SA, Eggermont J, Yao Z, Aevermann BD, Aldridge AI, Bartlett A, Bertagnolli D, Casper T, Castanon RG, Crichton K, … Lein ES (2021) Comparative cellular analysis of motor cortex in human, marmoset and mouse. *Nature*, 598, 111–119. https://doi.org/10.1038/s41586-021-03465-8

Bengtsson Gonzales C, Hunt S, Munoz-Manchado AB, McBain CJ, Hjerling-Leffler J (2020) Intrinsic electrophysiological properties predict variability in morphology and connectivity among striatal Parvalbumin-expressing Pthlh-cells. *Scientific Reports*, 10, 15680. https://doi.org/10.1038/s41598-020-72588-1

Berryer MH, Chattopadhyaya B, Xing P, Riebe I, Bosoi C, Sanon N, Antoine-Bertrand J, Lévesque M, Avoli M, Hamdan FF, Carmant L, Lamarche-Vane N, Lacaille JC, Michaud JL, Di Cristo G (2016) Decrease of SYNGAP1 in GABAergic cells impairs inhibitory synapse connectivity, synaptic inhibition and cognitive function. *Nature Communications*, 7, 13340. https://doi.org/10.1038/ncomms13340

Berryer MH, Hamdan FF, Klitten LL, Møller RS, Carmant L, Schwartzentruber J, Patry L, Dobrzeniecka S, Rochefort D, Neugnot-Cerioli M, Lacaille JC, Niu Z, Eng CM, Yang Y, Palardy S, Belhumeur C, Rouleau GA, Tommerup N, Immken L, … Di Cristo G (2013) Mutations in SYNGAP1 cause intellectual disability, autism, and a specific form of epilepsy by inducing haploinsufficiency. *Human Mutation* 34, 385–394. https://doi:10.1002/humu.22248

Bertero A, Feyen PLC, Zurita H, Apicella A (2019) A non-canonical cortico-amygdala inhibitory loop. *Journal of Neuroscience*, 39, 8424–8438. https://doi.org/10.1523/JNEUROSCI.1515-19.2019

Birtele M, Del Dosso A, Xu T, Nguyen T, Wilkinson B, Hosseini N, Nguyen S, Urenda JP, Knight G, Rojas C, Flores I, Atamian A, Moore R, Sharma R, Pirrotte P, Ashton RS, Huang EJ, Rumbaugh G, Coba MP, Quadrato G (2023). Non-synaptic function of the autism spectrum disorder-associated gene SYNGAP1 in cortical neurogenesis. *Nature Neuroscience* 26, 2090-2103. doi: 10.1038/s41593-023-01477-3.

Bourdeau ML, Morin F, Laurent CE, Azzi M, Lacaille JC (2007) Kv4. 3-mediated A-type K+ currents underlie rhythmic activity in hippocampal interneurons. *The Journal of Neuroscience*, 27, 1942– 1953. https://doi.org/10.1523/JNEUROSCI.3208-06.2007

Cardin JA, Carlén M, Meletis K, Knoblich U, Zhang F, Deisseroth K, Tsai LH, Moore CI (2009) Driving fast-spiking cells induces gamma rhythm and controls sensory responses. *Nature*, 459, 663–667. https:// doi.org/10.1038/nature08002

Carlén M, Meletis K, Siegle JH, Cardin JA, Futai K, Vierling-Claassen D, Rühlmann C, Jones SR, Deisseroth K, Sheng M, Moore CI, Tsai LH (2012) A critical role for NMDA receptors in parvalbumin interneurons for gamma rhythm induction and behavior. *Molecular Psychiatry*, 17, 537–548. https://doi.org/10.1038/mp.2011.31

Carreño-Muñoz MI, Chattopadhyaya B, Agbogba K, Côté V, Wang S, Lévesque M, Avoli M, Michaud JL, Lippé S, Di Cristo G (2022) Sensory processing dysregulations as reliable translational biomarkers in syngap1 haploinsufficiency. *Brain*, 145, 754–69. https:// doi.org/10.1093/brain/awab329

Ceballo S, Piwkowska Z, Bourg J, Daret A, Bathellier B (2019) Targeted cortical manipulation of auditory perception. *Neuron*, 104, 1168-1179.e5. https://doi.org/10.1016/j.neuron.2019.09.043

Chai R, Zhang Y, Xin Y, Deng L, Xu N (2022) Somatostatin interneurons in auditory cortex regulate sensory representations and contribute to auditory perception. *BioRxiv* https://doi.org/10.1101/2022.07.06.498950

Chen IW, Helmchen F, Lütcke H (2015) Specific early and late oddball-evoked responses in excitatory and inhibitory neurons of mouse auditory cortex. *The Journal of Neuroscience*, 35, 12560-12573. https://doi.org/10.1523/JNEUROSCI.2240-15.2015

Chiu CQ, Lur G, Morse TM, Carnevale NT, Ellis-Davies GCR, Higley MJ (2013) Compartmentalization of GABAergic inhibition by dendritic spines. *Science*, 340, 759–762. https://doi.org/10.1126/science.1234274

Christensen RK, Lindén H, Nakamura M, Barkat TR (2019) White noise background improves tone discrimination by suppressing cortical tuning curves. *Cell Reports*, 29, 2041-2053.e4. https://doi.org/10.1016/j.celrep.2019.10.049

Clement JP, Aceti M, Creson TK, Ozkan ED, Shi Y, Reish NJ, Almonte AG, Miller BH, Wiltgen BJ, Miller CA, Xu X, Rumbaugh G (2012) Pathogenic SYNGAP1 mutations impair cognitive development by disrupting maturation of dendritic spine synapses. *Cell*, 151, 709-723. https://doi.org/10.1016/j.cell.2012.08.045

Clement JP, Ozkan ED, Aceti M, Miller CA, Rumbaugh G (2013) SYNGAP1 links the maturation rate of excitatory synapses to the duration of critical-period synaptic plasticity. *The Journal of Neuroscience*, 33, 10447-10452. https://doi.org/10.1523/JNEUROSCI.0765-13.2013

Cohen L, Mizrahi A (2015) Plasticity during motherhood: changes in excitatory and inhibitory layer 2/3 neurons in auditory cortex. *The Journal of Neuroscience*, 35, 1806-1815. https://doi.org/10.1523/JNEUROSCI.1786-14.2015

Creson TK, Rojas C, Hwaun E, Vaissiere T, Kilinc M, Jimenez-Gomez A, Holder JL, Tang J, Colgin LL, Miller CA, Rumbaugh G (2019) Re-expression of SynGAP protein in adulthood improves translatable measures of brain function and behavior. *ELife*, 8, e46752. https://doi.org/10.7554/eLife.46752

Dehorter N, Ciceri G, Bartolini G, Lim L, del Pino I, Marín O (2015) Tuning of fast-spiking interneuron properties by an activity-dependent transcriptional switch. *Science*, 349, 1216–1220. https://doi.org/10.1126/science.aab3415

Ekins TG, Mahadevan V, Zhang Y, D'Amour JA, Akgül G, Petros TJ, McBain CJ (2020) Emergence of non-canonical parvalbumin-containing interneurons in hippocampus of a murine model of type I lissencephaly. *ELife*, 9, e62373. https://doi.org/10.7554/eLife.62373

Favuzzi E, Marques-Smith A, Deogracias R, Winterflood CM, Sánchez-Aguilera A, Mantoan L, Maeso P, Fernandes C, Ewers H, Rico B (2017) Activity-dependent gating of parvalbumin interneuron function by the perineuronal net protein brevican. *Neuron*, 95, 639-655.e10. https://doi.org/https://doi.org/10.1016/j.neuron.2017.06.028

Gamache TR, Araki Y, Huganir RL (2020) Twenty years of SynGAP research: from synapses to cognition. *The Journal of Neuroscience*, 40, 1596-1605. https://doi.org/10.1523/JNEUROSCI.0420-19.2020

Goldberg EM, Clark BD, Zagha E, Nahmani M, Erisir A, Rudy B (2008) K+ Channels at the axon initial segment dampen near-threshold excitability of neocortical fast-spiking GABAergic interneurons. *Neuron*, 58, 387–400. https://doi.org/10.1016/j.neuron.2008.03.003

Gonçalves AM, Monteiro P (2023) Autism Spectrum Disorder and auditory sensory alterations: a systematic review on the integrity of cognitive and neuronal functions related to auditory processing. *Journal of Neural Transmission*, 130, 325–408. https://doi.org/10.1007/s00702-023-02595-9

Gothner T, Gonçalves PJ, Sahani M, Linden JF, Hildebrandt KJ (2021) Sustained activation of PV+ interneurons in core auditory cortex enables robust divisive gain control for complex and naturalistic stimuli. *Cerebral Cortex*, 31, 2364-2381. https://doi:10.1093/cercor/bhaa347

Hamdan FF, Gauthier J, Spiegelman D, Noreau A, Yang Y, Pellerin S, Dobrzeniecka S, Côté M, Perreau-Linck E, Carmant L, D'Anjou G, Fombonne É, Addington AM, Rapoport JL, Delisi LE, Krebs MO, Mouaffak F, Joober R, Mottron L, … Michaud JL (2009) Mutations in SYNGAP1 in autosomal nonsyndromic mental retardation. *New England Journal of Medicine*, 360, 599–605. https://doi.org/10.1056/NEJMoa0805392

Hamilton LS, Sohl-Dickstein J, Huth AG, Carels VM, Deisseroth K, Bao S (2013). Optogenetic activation of an inhibitory network enhances feedforward functional connectivity in auditory cortex. *Neuron*, 80, 1066–1076. https://doi.org/10.1016/j.neuron.2013.08.017

Helm J, Akgul G, Wollmuth LP (2013) Subgroups of parvalbumin-expressing interneurons in layers 2/3 of the visual cortex. *Journal of Neurophysiology*, 109, 1600–1613. https://doi.org/10.1152/jn.00782.2012

Henton A, Zhao Y, Tzounopoulos T (2023) A Role for KCNQ channels on cell type-specific plasticity in mouse auditory cortex after peripheral damage. *The Journal of Neuroscience*, 43, 2277-2290. https://doi.org/10.1523/JNEUROSCI.1070-22.2023

Ji X, Zingg B, Mesik L, Xiao Z, Zhang LI, Tao HW (2016) Thalamocortical innervation pattern in mouse auditory and visual cortex: laminar and cell-type specificity. *Cerebral Cortex*, 26, 2612–2625. https://doi.org/10.1093/cercor/bhv099

Kawaguchi Y, Kubota Y (1997) GABAergic cell subtypes and their synaptic connections in rat frontal cortex. *Cerebral Cortex*, 7, 476–486. https://doi.org/10.1093/cercor/7.6.476

Keller CH, Kaylegian K, Wehr M (2018) Gap encoding by parvalbumin-expressing interneurons in auditory cortex. *Journal of Neurophysiology*, 120, 105–114. https://doi.org/10.1152/jn.00911.2017

Khlaifia A, Jadhav V, Danik M, Badra T, Berryer MH, Dionne-Laporte A, Chattopadhyaya B, Di Cristo G, Lacaille JC, Michaud JL (2023) Disruption induced by recombination between inverted loxP sites is associated with hippocampal interneuron dysfunction. *Eneuro*, 10, ENEURO.0475-22.2023. https://doi.org/10.1523/ENEURO.0475-22.2023

Kilgard MP, Merzenich MM (1999) Distributed representation of spectral and temporal information in rat primary auditory cortex. *Hearing Research*, 134, 16–28. https://doi.org/10.1016/S0378-5955(99)00061-1

King AJ, Teki S, Willmore, BDB (2018) Recent advances in understanding the auditory cortex. *F1000Research*, 7. https://doi.org/10.12688/f1000research.15580.1

Kratz MB, Manis PB (2015) Spatial organization of excitatory synaptic inputs to layer 4 neurons in mouse primary auditory cortex. *Frontiers in Neural Circuits,* 9, 17. https://www.frontiersin.org/articles/10.3389/fncir.2015.00017

Lakunina AA, Nardoci MB, Ahmadian Y, Jaramillo S (2020) Somatostatin-expressing interneurons in the auditory cortex mediate sustained suppression by spectral surround. *The Journal of Neuroscience*, 40, 3564-3575. https://doi:10.1523/JNEUROSCI.1735-19.2020

Letzkus JJ, Wolff SBE, Meyer EMM, Tovote P, Courtin J, Herry C, Lüthi A (2011) A disinhibitory microcircuit for associative fear learning in the auditory cortex. *Nature*, 480, 331–335. https://doi.org/10.1038/NATURE10674

Levy RB, Reyes AD (2012) Spatial profile of excitatory and inhibitory synaptic connectivity in mouse primary auditory cortex. *The Journal of Neuroscience*, 32, 5609-5619. https://doi.org/10.1523/JNEUROSCI.5158-11.2012

Li L, Ji X, Liang F, Li Y, Xiao Z, Tao HW, Zhang LI (2014) A feedforward inhibitory circuit mediates lateral refinement of sensory representation in upper layer 2/3 of mouse primary auditory cortex. *The Journal of Neuroscience*, 34, 13670-13683. https://doi.org/10.1523/JNEUROSCI.1516-14.2014

https://doi.org/10.1523/JNEUROSCI.1516-14.2014

Li LY, Xiong XR, Ibrahim LA, Yuan W, Tao HW, Zhang LI (2015) Differential receptive field properties of parvalbumin and somatostatin inhibitory neurons in mouse auditory cortex. *Cerebral Cortex*, 25, 1782–1791. https://doi.org/10.1093/CERCOR/BHT417

Meng X, Kao JPY, Lee HK, Kanold PO (2017) Intracortical circuits in thalamorecipient layers of auditory cortex refine after visual deprivation. *Eneuro*, 4, ENEURO.0092-17.2017. https://doi.org/10.1523/ENEURO.0092-17.2017

Michaelson SD, Ozkan ED, Aceti M, Maity S, Llamosas N, Weldon M, Mizrachi E, Vaissiere T, Gaffield MA, Christie JM, Holder JL, Miller CA, Rumbaugh G (2018) SYNGAP1 heterozygosity disrupts sensory processing by reducing touch-related activity within somatosensory cortex circuits. *Nature Neuroscience*, 21, 1–13. https://doi.org/10.1038/s41593-018-0268-0

Moore, A K, Wehr M (2013) Parvalbumin-expressing inhibitory interneurons in auditory cortex are well-tuned for frequency. The Journal of Neuroscience, 33, 13713-13723. https://doi:10.1523/JNEUROSCI.0663-13.2013

Myatt D, Hadlington T, Ascoli G, Nasuto S (2012) Neuromantic – from semi-manual to semi-automatic reconstruction of neuron morphology. *Frontiers in Neuroinformatics*, 6, 4. https://doi:10.3389/fninf.2012.00004

Nassar M, Simonnet J, Lofredi R, Cohen I, Savary E, Yanagawa Y, Miles R, Fricker D (2015) Diversity and overlap of Parvalbumin and Somatostatin expressing interneurons in mouse presubiculum. *Frontiers in Neural Circuits*, 9, 20. https://doi:10.3389/fncir.2015.00020

Nocon JC, Gritton HJ, James NM, Mount RA, Qu Z, Han X, Sen K(2023) Parvalbumin neurons enhance temporal coding and reduce cortical noise in complex auditory scenes. *Communications Biology*, 6, 751. https://doi.org/10.1038/s42003-023-05126-0

Okaty BW, Miller MN, Sugino K, Hempel CM, Nelson SB (2009) Transcriptional and electrophysiological maturation of neocortical fast-spiking GABAergic interneurons. *The Journal of Neuroscience*, 29, 7040-7052. https://doi:10.1523/JNEUROSCI.0105-09.2009

Ozkan ED, Creson TK, Kramár EA, Rojas C, Seese RR, Babyan AH, Shi Y, Lucero R, Xu X, Noebels JL, Miller CA, Lynch G, Rumbaugh G (2014) Reduced cognition in Syngap1 mutants is

caused by isolated damage within developing forebrain excitatory neurons. *Neuron*, 82, 1317–1333. https://doi.org/10.1016/j.neuron.2014.05.015

Phillips EAK, Hasenstaub AR (2016) Asymmetric effects of activating and inactivating cortical interneurons. *ELife*, 5, e18383. https://doi.org/10.7554/eLife.18383.

Pi HJ, Hangya B, Kvitsiani D, Sanders JI, Huang ZJ, Kepecs A (2013) Cortical interneurons that specialize in disinhibitory control. *Nature*, 503, 521–524. https://doi.org/10.1038/NATURE12676

Povysheva NV, Gonzalez-Burgos G, Zaitsev AV, Kröner S, Barrionuevo G, Lewis DA, Krimer LS (2006) Properties of excitatory synaptic responses in fast-spiking interneurons and pyramidal cells from monkey and rat prefrontal cortex. *Cerebral Cortex*, 16, 541–552. https://doi.org/10.1093/cercor/bhj002

Rock C, Zurita H, Lebby S, Wilson CJ, Apicella AJ (2018) Cortical circuits of callosal GABAergic neurons. *Cerebral Cortex*, 28, 1154–1167. https://doi.org/10.1093/CERCOR/BHX025

Rumbaugh G, Adams JP, Kim JH, Huganir RL (2006) SynGAP regulates synaptic strength and mitogen-activated protein kinases in cultured neurons. *Proceedings of the National Academy of Sciences*, 103, 4344–4351. https://doi.org/10.1073/pnas.0600084103

Schreiner CE, Winer JA (2007) Auditory cortex mapmaking: principles, projections, and plasticity. *Neuron*, 56, 356–365. https://doi.org/10.1016/j.neuron.2007.10.013

Serôdio P, Rudy B (1998) Differential expression of Kv4 K+ channel subunits mediating subthreshold transient K+ (A-type) currents in rat brain. *Journal of Neurophysiology*, 79, 1081–1091. https://doi.org/10.1152/jn.1998.79.2.1081

Seybold BA, Phillips EAK, Schreiner CE, Hasenstaub AR (2015) Inhibitory actions unified by network integration. *Neuron*, 87, 1181–1192. https://doi.org/10.1016/j.neuron.2015.09.013

Sinclair D, Oranje B, Razak KA, Siegel SJ, Schmid S (2017) Sensory processing in autism spectrum disorders and Fragile X syndrome—From the clinic to animal models. *Neuroscience and biobehavioral reviews,* 76, 235-253. https://doi:10.1016/j.neubiorev.2016.05.029

Spencer K (2012) Baseline gamma power during auditory steady-state stimulation in schizophrenia. *Frontiers in Human Neuroscience*, 5, 190. https://doi.org/10.3389/fnhum.2011.00190

Studer F, Barkat TR (2022) Inhibition in the auditory cortex. *Neuroscience & Biobehavioral Reviews*, 132, 61–75. https://doi.org/10.1016/J.NEUBIOREV.2021.11.021

Su P, Lai TKY, Lee FHF, Abela AR, Fletcher PJ, Liu F (2019) Disruption of SynGAP–dopamine D1 receptor complexes alters actin and microtubule dynamics and impairs GABAergic interneuron migration. *Science Signaling*, 12, eaau9122. https://doi.org/10.1126/scisignal.aau9122

Sullivan BJ, Ammanuel S, Kipnis PA, Araki Y, Huganir RL, Kadam SD (2020) Low-dose perampanel rescues cortical gamma dysregulation associated with parvalbumin interneuron GluA2 upregulation in epileptic Syngap1+/− mice. *Biological Psychiatry*, 87, 829-842. https://doi.org/10.1016/j.biopsych.2019.12.025

Szymanski FD, Garcia-Lazaro JA, Schnupp JWH (2009) Current source density profiles of stimulus-specific adaptation in rat auditory cortex. *Journal of Neurophysiology*, 102, 1483–1490. https://doi.org/10.1152/jn.00240.2009

Tremblay R, Lee S, Rudy B (2016) GABAergic interneurons in the neocortex: from cellular properties to circuits. *Neuron*, 91, 260–292. https://doi.org/10.1016/j.neuron.2016.06.033

Ulanovsky N, Las L, Nelken I (2003) Processing of low-probability sounds by cortical neurons. Nature Neuroscience, 6, 391–398. https://doi.org/10.1038/nn1032

Wang H, Kunkel DD, Schwartzkroin PA, Tempel BL (1994) Localization of Kv1.1 and Kv1.2, two K channel proteins, to synaptic terminals, somata, and dendrites in the mouse brain. *The Journal of Neuroscience*, 14, 4588-4599. https://doi.org/10.1523/JNEUROSCI.14-08-04588.1994

Wang W, Deng D, Jenkins K, Zinsmaier AK, Zhou Q, Bao S (2022) Correlation of electrophysiological and gene transcriptional dysfunctions in single cortical parvalbumin neurons after noise trauma. *Neuroscience*, 482, 87–99. https://doi.org/10.1016/j.neuroscience.2021.12.006

Wehr M, Zador AM (2003) Balanced inhibition underlies tuning and sharpens spike timing in auditory cortex. *Nature*, 426, 442–446. https://doi.org/10.1038/nature02116

Yavorska I, Wehr M (2016) Somatostatin-expressing inhibitory interneurons in cortical circuits. *Frontiers in Neural Circuits*, 10, 76. https://doi.org/10.3389/fncir.2016.00076

Yee JX, Rastani A, Soden ME (2022) The potassium channel auxiliary subunit Kvβ2 (Kcnab2) regulates Kv1 channels and dopamine neuron firing. *Journal of Neurophysiology*, 128, 62–72. https://doi.org/10.1152/jn.00194.2022

Zhang M, Eichhorn SW, Zingg B, Yao Z, Cotter K, Zeng H, Dong H, Zhuang X (2021) Spatially resolved cell atlas of the mouse primary motor cortex by MERFISH. *Nature*, 598, 137–143. https://doi.org/10.1038/s41586-021-03705-x

Zhao C, Kao JPY, Kanold PO (2009) Functional excitatory microcircuits in neonatal cortex connect thalamus and layer 4. *The Journal of Neuroscience*, 29, 15479-15488. https://doi.org/10.1523/JNEUROSCI.4471-09.2009

Zurita H, Feyen PLC, Apicella AJ (2018) Layer 5 callosal parvalbumin-expressing neurons: a distinct functional group of GABAergic neurons. *Frontiers in Cellular Neuroscience*, 12, 53. https://doi.org/10.3389/fncel.2018.00053

Supplementary Figures

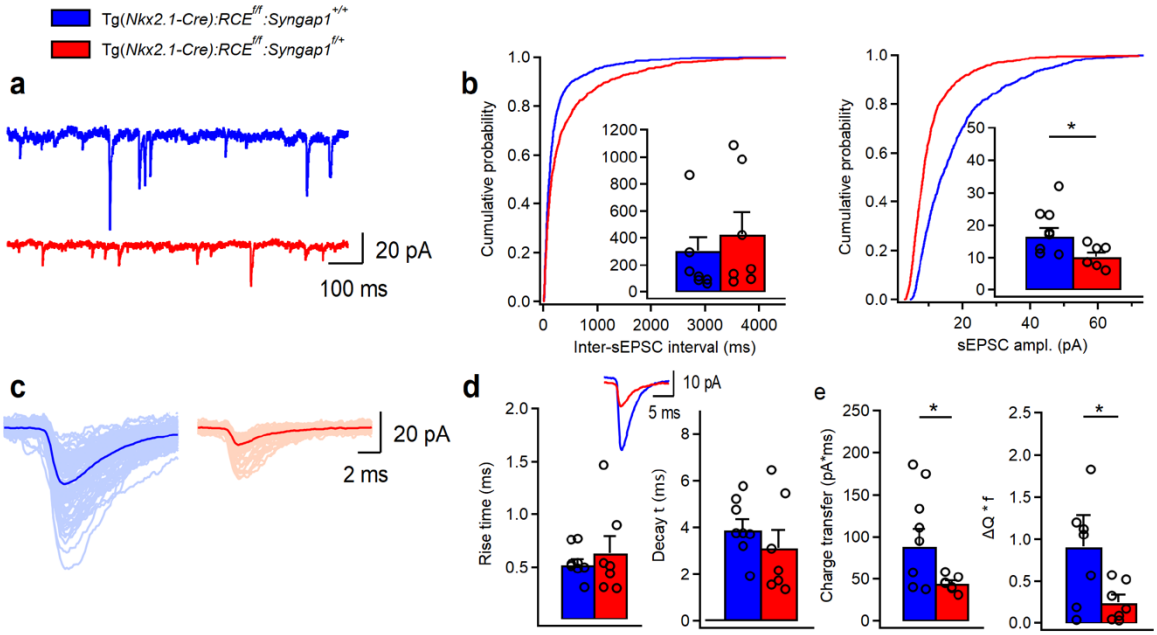

Supplementary Figure 1. sEPSC amplitude is reduced in LIV SST+ cells in Tg(*Nkx2.1-Cre*):*RCE*$^{f/f}$:*Syngap1*$^{f/+}$ mice (**a**) Representative traces of sEPSCs recorded in SST+ cells from control (blue, n=8 cells, 5 mice) and cHet mice (red, n=7 cells, 5 mice). (**b**) Cumulative probability plots show a significant decrease in the amplitude (***p<0.001, LMM) and no change in the inter-sEPSC interval (LMM, p=0.124). Insets illustrate significant differences in the sEPSC amplitude for inter-cell mean comparison (*p=0.010, LMM) and no difference for inter-sEPSC interval (p=0.236, LMM). (**c**) Representative examples of individual sEPSC events (100 pale sweeps) and average traces (bold trace) detected in SST+ cells of control and cHet mice. (**d**) Superimposed scaled traces (left top) and summary bar graphs for a group of cells (bottom) show no significant differences in the sEPSCs kinetics (p=0.562, LMM for rise time, and p=0.281, LMM for decay time). (**e**) Summary bar graphs showing a significant decrease in cHet mice for inter-cell mean charge transfer

(*p=0.015, LMM, left) and for the charge transfer when frequency of events is considered (*p>0.030, LMM).

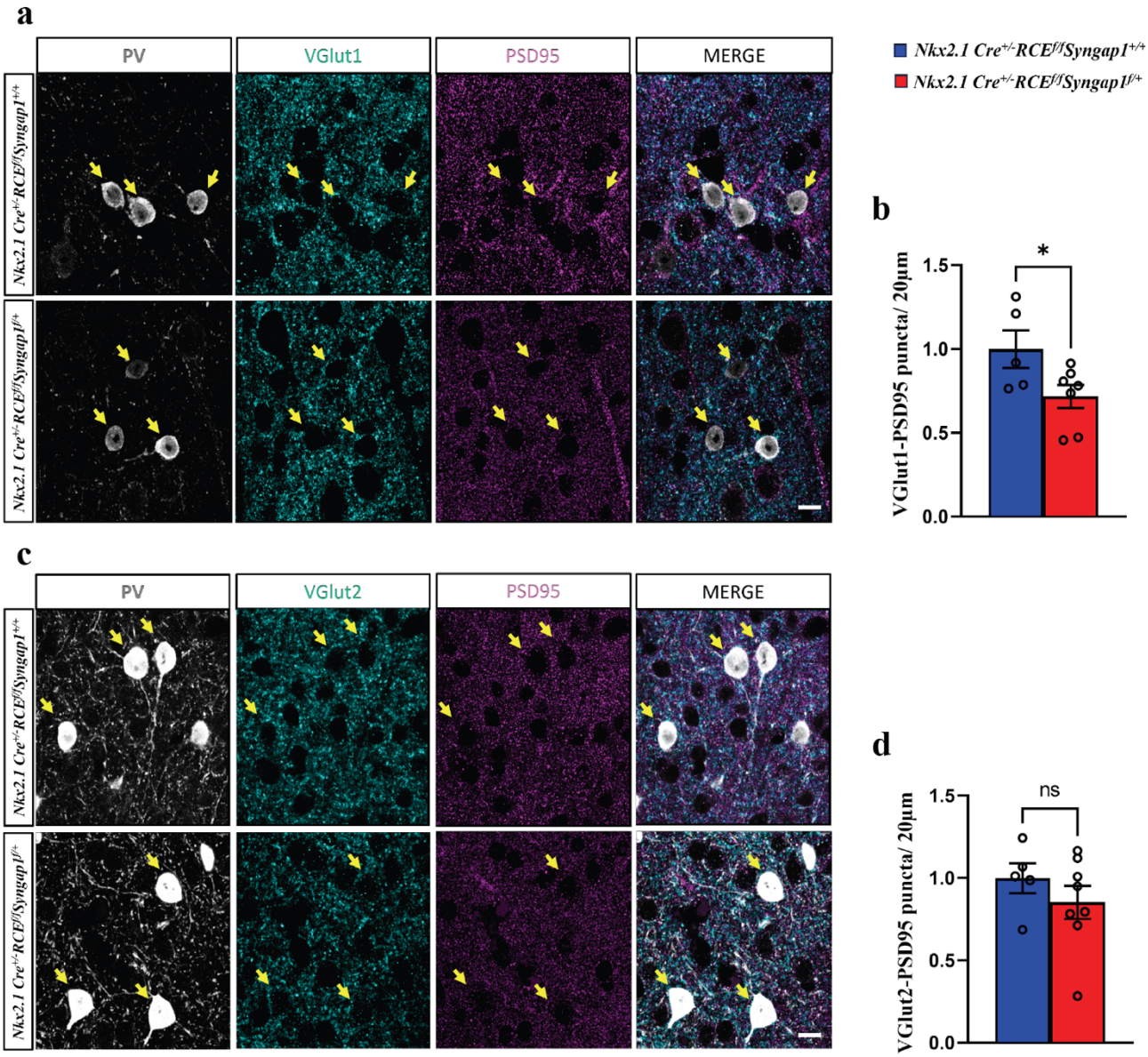

Supplementary Figure 2. *Syngap1* haploinsufficiency reduces the density of local vGlut1 excitatory inputs without affecting VGlut2 thalamocortical inputs to PV+ cell somata. (**a**) Representative images of auditory cortex immunolabelled for PV (grey), VGlut1 (cyan), PSD95 (magenta) in control (*Nkx2.1 Cre; Syngap1*$^{+/+}$) and cHet (*Nkx2.1 Cre; Syngap1*$^{flox/+}$) adult mice. Scale bar: 10 µm (**b**) Quantification of the density of perisomatic puncta colocalizing both VGlut1 and PSD95 normalised to controls (Unpaired t-test *p= 0.0447). Number of mice: n=5 mice for control and n=7 for cHet. (**c**) Representative images of auditory cortex immunolabelled for PV

(grey), VGlut2 (cyan), PSD95 (magenta). Scale bar: 10 µm (**d**) Quantification of of the density of perisomatic puncta colocalizing both VGlut2 and PSD95 normalised to controls (Unpaired t-test p= 0.3345). Number of mice: n=5 mice for control and n=8 for cHet. Yellow arrows indicate PV cell somata. Bar graphs represent mean ± SEM. ns $p > 0.05$ ns, not significant, *$p < 0.05$, **$p < 0.01$, ***$p < 0.001$.

Supplemental data Francavilla et al., 2024

Results of statistical analysis performed with LMM and Mann Whitney or t-test for each data set

Yellow underlight indicates significance

Table 1. sEPSCs and mEPSCs in PV+ cells from control Vs PV+ cells from cHet mice. Related to Fig. 1

	Control	cHet	LMM	Unpaired-t test or MWT
sEPSC ampl.	14.68 ±0.97 pA (n=28, 11 anim.)	10.68±0.92 pA (n=28, 11 anim.)	F=4.269 p=0.044*	MWT p=0.002**
AUC sEPSC	61.67±8.56 pA x ms (n=28, 11 anim.)	38.6±5.1 pA x ms (n=28, 11 anim.) *	F=4.885 p=0.064	MWT p=0.004**
sEPSC freq.	12.09±1.81 Hz (n=28, 11 anim.)	9.91±1.66 Hz (n=28, 11 anim.)	F=0.177 p=0.676	MWT p=0.325
ΔQ * f	0.65±0.10 (n=28, 11 anim.)	0.43±0.09 (n=28, 11 anim.)	F=1.540 p=0.220	MWT p=0.040*
Rise time sEPSC	0.42±0.03 ms (n=28, 11 anim.)	0.38±0.02 ms (n=28, 11 anim.)	F=0.900 p=0.350	MWT p=0.416
Decay time sEPSC	2.38±0.30 ms (n=28, 11 anim.)	1.96±0.16 ms (n=28, 11 anim.)	F=0.635 p=0.429	MWT p=0.857
mEPSC ampl.	12.61±0.88 pA (n=18, 6 anim.)	10.5±1.31 pA (n=8, 4 anim.)	F=1.859 p=0.185	Unpaired-t test p=0.203
mEPSC freq.	10.05 ±2.1 Hz (n=18, 6 anim.)	6.92 ±3.04 Hz (n=8, 4 anim.)	F=0.938 p=0.354	MWT p=0.101
AUC mEPSC	58.41±7.51 pA x ms (n=18, 6 anim.)	34.41±4.25 pA x ms (n=8, 4 anim.)	F=3.850 p=0.069	MWT p=0.028*
mEPSC freq.	10.05±2.09 Hz (n=18, 6 anim.)	6.92±3.04 Hz (n=8, 4 anim.)	F=0.938 p=0.354	MWT p=0.101
Quantal content	1.32±0.14 (n=10, 4 anim.)	1.10±0.27 (n=8, 4 anim.)	F=1.616 p=0.222	Unpaired-t test p=0.248
ΔQ * f	0.62±0.15 (n=18, 6 anim.)	0.25±0.12 ms (n=8, 4 anim.)	F=2.369 p=0.137	MWT p=0.043*
Rise time mEPSC	0.45±0.05 ms (n=18, 6 anim.)	0.39±0.04 ms (n=8, 4 anim.)	F=0.366 p=0.556	MWT p=0.867
Decay time mEPSC	2.69±0.49 ms (n=18, 6 anim.)	2.20±0.36 ms (n=8, 4 anim.)	F=0.302 p=0.591	MWT p=0.824

Table 2. sIPSCs and mIPSCs in PV+ cells from control Vs PV+ cells from cHet mice. Related to Fig. 2

	Control	cHet	LMM	Unpaired-t test or MWT
sIPSC ampl.	25.10±1.30 pA (n=27, 8 anim.)	19.59±1.07 pA (n=24, 7 anim.)	F=10.758 p=0.002**	MWT p=0.002**
AUC sIPSC	135.49±9.03 pA x ms (n=27, 8 anim.)	120.42±8.74 pA x ms (n=24, 7 anim.)	F=1.452 p=0.234	MWT p=0.282
sIPSC freq.	9.94±1.28 Hz (n=27, 8 anim.)	14.29±1.82 Hz (n=24, 7 anim.)	F=3.031 p=0.102	MWT p=0.083
ΔQ * f sIPSC	1.28±0.16 (n=27, 8 anim.)	1.53±0.15 (n=24, 4 anim.)	F=1.227 p=0.273	MWT p=0.165
sIPSC rise time	0.39±0.02 ms (n=27, 8 anim.)	0.48±0.04 ms (n=24, 7 anim.)	F=2.794 p=0.113	MWT p=0.026*
sIPSC decay time	4.26±0.36 ms (n=27, 8 anim.)	4.07±0.26 ms (n=24, 7 anim.)	F=0.287 p=0.602	MWT p=0.940
mIPSC ampl.	21.55±1.08 pA (n=25, 8 anim.)	19.38±1.25 pA (n=24, 7 anim.)	F=1.726 p=0.195	MWT p=0.204
AUC mIPSC	127.89±9.56 pA x ms (n=25, 8 anim.)	133.35±10.26 pA x ms (n=24, 7 anim.)	F=0.120 p=0.374	Unpaired-t test p=0.699
mIPSC freq.	12.58±1.60 Hz (n=25, 8 anim.)	15.76±2.25 Hz (n=24, 7 anim.)	F=1.400 p=0.243	MWT p=0.407
Quantal content	1.19±0.05 (n=25, 8 anim.)	1.06±0.05 (n=22, 7 anim.)	F=3.077 p=0.086	Unpaired-t test p=0.092
ΔQ * f mIPSC	1.43±0.14 (n=25, 8 anim.)	2.02±0.34 (n=24, 7 anim.)	F=2.809 p=0.100	MWT p=0.430
mIPSC rise time	0.38±0.01 ms (n=25, 8 anim.)	0.49±0.03 ms (n=24, 7 anim.)	F=2.907 p=0.103	MWT p=0.015*
mIPSC decay time	4.45±0.36 ms (n=25, 8 anim.)	4.94±0.35 ms (n=24, 7 anim.)	F=0.293 p=0.597	MWT p=0.352

Table 3. eAMPA and eNMDA currents in LIV PV+ cells from control Vs cHet mice. Related to Fig. 3

	Control	cHet	LMM	MWT or unpaired-t test
Failure rate (%)	7.75±2.95 (n=16, 7 anim.)	10.57±3.89 pA (n=14, 8 anim.)	F=0.367 p=0.550	MWT p=0.548
Minimal eAMPA	32.33±5.61 pA (n=16, 7 anim.)	17.67±2.51 pA (n=14, 8 anim.)	F=5.155 p=0.031*	MWT p=0.048*
AUC eAMPA	150.28±20.25 pA x ms (n=16, 7 anim.)	95.86±11.70 pA x ms (n=14, 8 anim.)	F=5.017 p=0.033*	Unpaired-t test p=0.033*
Onset latencies eAMPA	4.27±0.11 ms (n=101, 7 anim.)	5.07±0.07 ms (n=114, 8 anim.)	F=5.261 p=0.023*	MWT p=0<0.001***
Rise time eAMPA	0.67±0.13 ms (n=16, 7 anim.)	0.90±0.09 ms (n=13, 7 anim.)	F=2.046 p=0.177	MWT p=0.018*
Decay time eAMPA	3.25±0.71 ms (n=16, 7 anim.)	3.71±0.49 ms (n=13, 7 anim.)	F=0.270 p=0.608	MWT p=0.167
eNMDA	42.15±13.31 pA (n=6, 3 anim.)	41.73±7.57 pA (n=6, 5 anim.)	F=0.002 p=0.969	Unpaired-t test p=0.979
eAMPA in NMDA containing BC	50.51±9.98 pA (n=6, 3 anim.)	14.9±2.37 pA (n=6, 5 anim.)	F=14.455 p=0.003**	MWT p=0.026*
NMDA/ AMPA	0.88±0.28 (n=6, 3 anim.)	2.82±0.39 (n=6, 5 anim.)	F=18.876 p=0.001**	MWT p=0.015*
Rise time eNMDA	2.42±0.55 ms (n=6, 3 anim.)	3.90±0.85 ms (n=6, 5 anim.)	F=1.846 p=0.228	MWT p=0.132
Decay time eNMDA	31.82±3.44 ms (n=6, 3 anim.)	63.33±21.22 ms (n=6, 5 anim.)	F=1.767 p=0.221	Unpaired-t test p=0.174

Table 4. Morphological properties of total PV+ cells population in control Vs cHet mice. Related to Fig. 4.

	PV cells in control (n=10) 7 animals	PV cells in cHet (n=12) 7 animals	LMM	MWT or unpaired-t test
Distance from pia (µm)	395.30 ± 16.30	391.91 ± 12.30	F=0.031 p=0.862	Unpaired-t test p=0.868
Soma perimeter (µm)	41.00 ± 1.53	39.95 ± 1.48	F=0.244 p=0.636	Unpaired-t test p=0.629
Number of dendrites	7.60 ± 0.65	6.00 ± 0.47	F=4.491 p=0.047*	Unpaired-t test p=0.057
Number of branching points	23.60 ± 2.86	30.83 ± 2.54	F=2.915 p=0.100	Unpaired-t test p=0.073
Number of terminals	33.10 ± 3.39	37.41 ± 2.62	F=0.609 p=0.456	Unpaired-t test p=0.319
Total dendritic lengt (µm)	2743.06 ± 258.45	2881.79 ± 153.36	F=0.021 p=0.887	Unpaired-test p=0.637
Dendritic surface area (μm^2)	9671.72 ± 1088.24	11111.15 ± 734.70	F=0.539 p=0.460	Unpaired-t test p=0.273
Number of intersections Sholl analysis	172.20 ± 8.66	180.66 ± 9.40	F=0.467 p=0.502	Unpaired-t test p=0.522

Table 5. Membrane properties of total PV+ cells population in control Vs cHet mice. Related to Fig. 5

	PV cells in control (n=33) 15 animals	PV cells in cHet (n=40) 17 animals	LMM	MWT or unpaired-t test
Resting membrane potential (mV)	-70.51 ± 0.85	-68.32 ± 0.86	F=3.293 p=0.081	Unpaired-t test p=0.102
Input resistance (MΩ)	275.51 ± 14.15	251.02 ± 12.31	F=1.767 p=0.188	MWT p=0.193
Membrane capacitance (pF)	29.00 ± 1.09	29.6 ± 0.87	F=1.767 p=0.188	Unpaired-t test p=0.193
Membrane time constant (ms)	7.88 ± 0.47	7.19 ± 0.30	F=1.679 p=0.199	MWT p=0.343
Rheobase current (pA)	129.09 ± 6.69	167.00 ± 9.37	F=9.256 p=0.004**	MWT p=0.002**
AP threshold (mV)	-42.57 ± 1.01	-35.29 ± 1.22	F=17.519 p<0.001***	Unpaired-test p<0.001***
AP amplitude (mV)	62.06 ± 1.36	56.99 ± 1.49	F=5.079 p=0.032*	Unpaired-t test p=0.011*
AP latency (ms)	31.44 ± 4.09	81.80 ± 17.00	F=7.136 p=0.009*	MWT p=0.058
AP half width (ms)	0.85 ± 0.04	0.73 ± 0.03	F=2.697 p=0.111	MWT p=0.026*
AP rise time (10-90 % ms)	0.38 ± 0.01	0.34 ± 0.01	F=3.266 p=0.080	MWT p=0.022*
AP decay time (10-90 % ms)	0.73 ± 0.04	0.62 ± 0.03	F=2.628 p=0.115	MWT p=0.019*
fAHP (mV)	-15.50 ± 0.57	-16.96 ± 0.57	F=3.281 p=0.074	Unpaired-t test p=0.056
fAHP (ms)	3.41 ± 0.16	2.97 ± 0.13	F=2.840 p=0.103	Unpaired-t test p=0.026*
I_h sag (mV)	0.75 ± 0.06	0.79 ± 0.10	F=0.100 p=0.752	MWT p=0.807
SAAR	0.78 ± 0.01 (n=32)	0.74 ± 0.02	F=1.887 p=0.174	MWT p=0.365
FFAR	1.35 ± 0.03 (n=32)	1.32 ± 0.02	F=0.473 p=0.496	Unpaired-t test p=0.523
Firing frequency at 2x rheobase current (Hz)	84.72 ± 4.98	101.6 ± 5.51	F=3.219 p=0.082	Unpaired-t test p=0.018*
Fmax (Hz)	163.88 ± 7.32 (n=27)	171.84 ± 7.62	F=0.457 p=0.507	MWT p=0.711
Fss (Hz)	102.33 ± 5.91 (n=27)	114.29 ± 5.68	F=1.421 p=0.243	MWT p=0.091

Table 6.1. Morphological properties of BC-short Vs BC-broad in control mice. Related to Fig. 6.

	BC-short (n=5) 4 animals	BC-broad (n=5) 4 animals	LMM	MWT or unpaired-t test
Distance from pia (µm)	398.20 ± 21.40	392.40 ± 27.06	F=0.035 p=0.856	Unpaired-t test p=0.871
Soma perimeter (µm)	39.20 ± 2.16	40.68 ± 0.75	F=7.473 p=0.053	Unpaired-t test p=0.538
Number of dendrites	7.60 ± 0.67	7.60 ± 1.20	F=0.001 p=1.000	Unpaired-t test p=1.000
Number of branching points	18.40 ± 1.63	28.80 ± 4.55	F=5.778 p=0.043*	Unpaired-t test p=0.064
Number of terminals	28.60 ± 1.56	37.60 ± 6.26	F=2.427 p=0.158	Unpaired-t test p=0.201
Total dendritic lengt (µm)	2304.84 ± 103.86	3181.27 ± 440.23	F=4.933 p=0.057	Unpaired-test p=0.089
Dendritic surface area (μm^2)	7483.76 ± 450.22	11859.68 ± 1653.16	F=9.263 p=0.016*	Unpaired-t test p=0.034*

Table 6.2. Morphological properties of BC-short Vs BC-broad in cHet mice. Related to Fig. 6.

	BC-short (n=6) 5 animals	BC-broad (n=6) 3 animals	LMM	MWT or unpaired-t test
Distance from pia (µm)	398.33 ± 18.6	385.50 ± 17.48	F=0.302 p=0.594	MWT p=0.598
Soma perimeter (µm)	41.40 ± 2.90	38.50 ± 0.66	F=1.143 p=0.310	Unpaired-t test p=0.352
Number of dendrites	5.00 ± 0.36	7.00 ± 0.68	F=7.998 p=0.032*	Unpaired-t test p=0.027*
Number of branching points	26.83 ± 3.50	34.83 ± 3.11	F=3.493 p=0.081	Unpaired-t test p=0.119
Number of terminals	32.50 ± 3.61	42.33 ± 2.77	F=5.509 p=0.040*	Unpaired-t test p=0.056
Total dendritic lengt (µm)	2618.24 ± 128.54	3145.34 ± 243.28	F=4.403 p=0.062	Unpaired-test p=0.084
Dendritic surface area (μm^2)	10864.15 ± 890.13	11358.15 ± 1248.32	F=0.125 p=0.731	Unpaired-t test p=0.754

Table 6.3. Morphological properties of BC-short in control Vs cHet mice. Related to Fig. 6.

	BC-short in control (n=5) 4 animals	BC-short in cHet (n=6) 4 animals	LMM	MWT or unpaired-t test
Distance from pia (µm)	398.20 ± 21.40	398.33 ± 18.64	F=0.001 p=0.996	Unpaired-t test p=0.996
Soma perimeter (µm)	39.20 ± 2.16	41.40 ± 2.90	F=0.488 p=0.523	Unpaired-t test p=0.572
Number of dendrites	7.60 ± 0.67	5.00 ± 0.36	F=15.364 p=0.002**	Unpaired-t test p=0.006*
Number of branching points	18.40 ± 1.63	26.83 ± 3.50	F=5.294 p=0.048*	Unpaired-t test p=0.072
Number of terminals	28.60 ± 1.56	32.50 ± 3.61	F=1.190 p=0.305	Unpaired-t test p=0.381
Total dendritic lengt (µm)	2304.84 ± 103.86	2618.24 ± 128.54	F=4.640 p=0.070	Unpaired-test p=0.099
Dendritic surface area (μm^2)	7483.76 ± 450.22	10864.15 ± 890.13	F=11.510 p=0.009*	Unpaired-t test p=0.011*

Table 6.4. Morphological properties of BC-broad in control Vs cHet mice. Related to Fig. 6.

	BC-broad in control (n=5) 4 animals	BC-broad in cHet (n=6) 3 animals	LMM	MWT or unpaired-t test
Distance from pia (µm)	392.40 ± 27.06	385.50 ± 17.40	F=0.060 p=0.812	Unpaired-t test p=0.812
Soma perimeter (µm)	40.68 ± 0.75	38.50 ± 0.66	F=5.789 p=0.040*	Unpaired-t test p=0.058
Number of dendrites	7.60 ± 1.20	7.00 ± 0.68	F=0.205 p=0.662	Unpaired-t test p=0.662
Number of branching points	28.80 ± 4.55	34.83 ± 3.11	F=1.266 p=0.290	Unpaired-t test p=0.290
Number of terminals	37.60 ± 6.26	42.33 ± 2.77	F=0.541 p=0.481	Unpaired-t test p=0.481
Total dendritic lengt (µm)	3181.27 ± 440.23	3145.34 ± 243.28	F=0.002 p=0.967	Unpaired-test p=0.942
Dendritic surface area (μm^2)	11859.68 ± 1653.16	11358.15 ± 1248.32	F=0.088 p=0.784	Unpaired-t test p=0.811

Table 7.1 Membrane properties of BC-short PV+ cells in control Vs cHet mice . Related to Fig. 7.

	BC-short in control (n=12) 9 animals	BC-short in cHet (n=24) 13 animals	LMM	MWT or unpaired-t test
Resting membrane potential (mV)	-72.33 ± 1.69	-69.79 ± 1.08	F=1.798 p=0.189	Unpaired-t test p=0.201
Input resistance (MΩ)	237.66 ± 19.98	242.00 ± 14.09	F=0.033 p=0.856	Unpaired-t test p=0.860
Membrane capacitance (pF)	33.08 ± 1.09	29.79 ± 0.87	F=3.331 p=0.077	MWT p=0.118
Membrane time constant (ms)	7.75 ± 0.58	6.96 ± 0.31	F=1.818 p=0.187	MWT p=0.199
Rheobase current (pA)	138.33 ± 12.42	190.00 ± 13.22	F=6.573 p=0.015*	Unpaired-t test p=0.018*
AP threshold (mV)	-43.38 ± 1.63	-33.95 ± 1.84	F=11.458 p=0.002**	Unpaired-test p=0.002**
AP amplitude (mV)	61.43 ± 1.94	54.60 ± 1.86	F=5.570 p=0.024*	Unpaired-t test p=0.028*
AP latency (ms)	36.36 ± 7.91	77.08 ± 22.70	F=1.631 p=0.210	MWT p=0.651
AP half width (ms)	0.63 ± 0.02	0.59 ± 0.02	F=0.779 p=0.386	MWT p=0.491
AP rise time (10-90 % ms)	0.31 ± 0.01	0.30 ± 0.01	F=0.146 p=0.705	MWT p=0.557
AP decay time (10-90 % ms)	0.52 ± 0.02	0.49 ± 0.02	F=0.832 p=0.368	MWT p=0.491
fAHP (mV)	-16.05 ± 1.06	-17.60 ± 0.77	F=1.423 p=0.241	Unpaired-t test p=0.254
fAHP (ms)	2.52 ± 0.10	2.50 ± 0.11	F=0.009 p=0.926	Unpaired-t test p=0.928
I_h sag (mV)	0.72 ± 0.12	0.80 ± 0.14	F=0.130 p=0.720	MWT p=0.973
SAAR	0.81 ± 0.02	0.72 ± 0.03	F=3.715 p=0.062	Unpaired-t test p=0.070
FFAR	1.31 ± 0.06	1.33 ± 0.04	F=0.082 p=0.776	Unpaired-t test p=0.782
Firing frequency at 2x rheobase current (Hz)	100.83 ± 7.55	116.66 ± 7.24	F=1.977 p=0.169	MWT p=0.065
Fmax (Hz)	191.97 ± 10.48 (n=11)	191.74 ± 10.14	F=0.001 p=0.989	MWT p=0.557
Fss (Hz)	124.23 ± 9.32 (n=11)	131.72 ± 6.92	F=0.411 p=0.526	MWT p=0.424

Table 7.2. Membrane properties of BC-broad PV+ cells in control Vs cHet mice. Related to Fig. 7.

	BC-broad in control (n=21) 12 animals	BC-broad in cHet (n=16) 11 animals	LMM	MWT or unpaired-t test
Resting membrane potential (mV)	-69.47 ± 0.87	-66.12 ± 1.25	F=5.895 p=0.023	Unpaired-t test p=0.030*
Input resistance (MΩ)	297.14 ± 19.98	264.56 ± 22.55	F=1.405 p=0.244	MWT p=0.219
Membrane capacitance (pF)	26.66 ± 1.30	29.31 ± 1.41	F=1.963 p=0.170	Unpaired-t test p=0.182
Membrane time constant (ms)	7.95 ± 0.67	7.52 ± 0.59	F=0.224 p=0.639	MWT p=0.748
Rheobase current (pA)	123.80 ± 7.76	132.50 ± 6.02	F=0.731 p=0.402	MWT p=0.258
AP threshold (mV)	-42.11 ± 1.31	-37.30 ± 1.18	F=7.313 p=0.010*	Unpaired-test p=0.013*
AP amplitude (mV)	62.42 ± 1.85	60.58 ± 2.28	F=0.140 p=0.713	Unpaired-t test p=0.530
AP latency (ms)	28.63 ± 4.63	88.86 ± 26.24	F=6.266 p=0.035*	MWT p=0.005*
AP half width (ms)	0.97 ± 0.04	0.94 ± 0.04	F=0.295 p=0.593	MWT p=0.701
AP rise time (10-90 % ms)	0.43 ± 0.01	0.40 ± 0.01	F=1.513 p=0.232	MWT p=0.238
AP decay time (10-90 % ms)	0.86 ± 0.04	0.82 ± 0.04	F=0.359 p=0.556	MWT p=0.453
fAHP (mV)	-15.19 ± 0.67	-16.01 ± 0.79	F=0.620 p=0.440	MWT p=0.794
fAHP (ms)	3.92 ± 0.16	3.67 ± 0.15	F=1.120 p=0.297	MWT p=0.389
I_h sag (mV)	0.77 ± 0.07	0.78 ± 0.12	F=0.189 p=0.667	MWT p=0.830
SAAR	0.75 ± 0.01	0.77 ± 0.02	F=1.715 p=0.202	Unpaired-t test p=0.567
FFAR	1.38 ± 0.03	1.32 ± 0.03	F=0.434 p=0.514	Unpaired-t test p=0.268
Firing frequency at 2x rheobase current (Hz)	75.52 ± 5.74 (n=20)	79.00 ± 4.50	F=0.984 p=0.331	MWT p=0.679
Fmax (Hz)	144.58 ± 6.73 (n=16)	141.98 ± 6.50	F=0.746 p=0.396	Unpaired-t test p=0.783
Fss (Hz)	87.27 ± 5.04 (n=16)	88.14 ± 4.85	F=1.061 p=0.312	Unpaired-t test p=0.902

Table 8. Membrane properties of total SST+ cells population in control Vs cHet mice. Related to Fig. 8

	SST+ cells in control (n=10) 7 animals	SST+ cells in cHet (n=12) 7 animals	LMM	MWT or unpaired-t test
Resting membrane potential (mV)	-69.40 ± 2.06	-67.58 ± 1.61	F=0.545 p=0.469	Unpaired-t test p=0.490
Input resistance (MΩ)	455.60 ± 72.14	475.41 ± 84.25	F=0.174 p=0.681	MWT p=0.869
Membrane capacitance (pF)	29.00 ± 1.09	29.6 ± 0.87	F=0.010 p=0.922	MWT p=0.868
Membrane time constant (ms)	15.58 ± 2.48	17.95 ± 3.74	F=0.281 p=0.602	MWT p=1.000
Rheobase current (pA)	52.00 ± 6.11	56.66 ± 9.15	F=0.181 p=0.675	MWT p=0.966
AP threshold (mV)	-44.53 ± 1.43	-47.55± 1.31	F=2.655 p=0.119	Unpaired-test p=0.136
AP amplitude (mV)	63.81 ± 2.61	68.50 ± 3.14	F=0.971 p=0.342	Unpaired-t test p=0.276
AP latency (ms)	93.39 ± 20.46	66.38 ± 7.67	F=1.925 p=0.081	Unpaired-t test p=0.201
AP half width (ms)	0.95 ± 0.09	0.94 ± 0.06	F=0.181 p=0.675	Unpaired-t test p=0.942
fAHP (mV)	-12.41 ± 0.85	-12.33 ± 1.10	F=0.004 p=0.953	Unpaired-t test p=0.955
I_h sag (mV)	1.94 ± 0.48	1.79 ± 0.32	F=0.070 p=0.794	MWT p=0.807
SAAR	0.82 ± 0.02	0.74 ± 0.04	F=2.020 p=0.170	MWT p=0.373
FFAR	2.22 ± 0.52	3.48 ± 1.01	F=2.668 p=0.141	MWT p=0.138
Firing frequency at 2x rheobase current (Hz)	36.60 ± 6.11	27.66 ± 1.36	F=2.649 p=0.119	MWT p=0.550
Fmax (Hz)	125.09 ± 9.89	123.98 ± 12.29 (n=11)	F=0.350 p=0.562	Unpaired-t test p=0.945
Fss (Hz)	59.42 ± 6.37	48.18 ± 6.31 (n=11)	F=0.533 p=0.471	Unpaired-t test p=0.226

Table 9. Membrane properties of PV+ in not-treated and α-DTX-treated PV+ cells in control and cHet. Related to Fig. 9

	(1) PV+ cells in control (n=9) 4 animals	(2) PV+ cells in control + α-DTX (n=11) 6 animals	(3) PV+ cells in cHet (n=23) 10 animals	(4) PV+ cells in cHet + α-DTX (n=18) 8 animals	LMM 1 Vs 2	Unpaired-t test or MWT 1 Vs 2	LMM 1 Vs 3	Unpaired-t test or MWT 1 Vs 3	LMM 1 Vs 4	Unpaired-t test or MWT 1 Vs 4	LMM 3 Vs 4	Unpaired-t test or MWT 3 Vs 4
Resting membrane potential (mV)	-66.77 ± 0.95	-71.09 ± 2.02	-68.91 ± 1.22	-66.83 ± 1.48	p=0.143	MWT p=0.158	p=0.293	MWT p=0.308	p=0.973	Unpaired-t test p=0.980	p=0.320	MWT p=0.220
Input resistance (MΩ)	281.11 ± 36.45	357.27 ± 63.01	274.13 ± 16.49	258.88 ± 20.92	p=0.313	MWT p=0.402	p=0.837	MWT p=0.817	p=0.560	Unpaired-t test p=0.575	p=0.555	MWT p=0.453
Membrane capacitance (pF)	26.77 ± 2.05	27.18 ± 1.36	28.82 ± 1.19	29.27 ± 1.50	p=0.860	Unpaired t-test p=0.867	p=0.366	Unpaired t-test p=0.381	p=0.322	Unpaired t-test p=0.341	p=0.874	Unpaired t-test p=0.813
Membrane time constant (ms)	7.33 ± 1.00	9.34 ± 1.56	7.71 ± 0.44	7.48 ± 0.63	p=0.500	MWT p=0.818	p=0.400	MWT p=0.367	p=0.602	MWT p=0.973	p=0.329	MWT p=0.761
Rheobase current (pA)	142.22 ± 16.48	123.63 ± 10.02	166.95 ± 13.22	144.44 ± 12.99	p=0.520	MWT p=0.430	p=0.308	MWT p=0.303	p=0.833	MWT p=0.979	p=0.263	Unpaired-t test p=0.240
AP threshold (mV)	-42.97 ± 2.68	-42.50 ± 1.60	-36.22 ± 1.67	-43.27 ± 2.30	p=0.871	Unpaired t-test p=0.878	*p=0.049	Unpaired-t test *p=0.041	p=0.940	Unpaired t-test p=0.937	*p=0.022	Unpaired t-test *p=0.015
AP amplitude (mV)	63.38 ± 2.54	64.10 ± 2.25	60.77 ± 1.75	61.89 ± 2.03	p=0.856	Unpaired t-test p=0.834	p=0.457	MWT p=0.294	p=0.690	Unpaired-t test p=0.664	p=0.672	Unpaired-t test p=0.679
AP latency (ms)	45.72 ± 11.66	54.87 ± 13.57	89.96 ± 21.41	56.67 ± 7.03	p=0.606	MWT p=0.362	p=0.686	MWT p=0.451	p=0.329	MWT p=0.130	p=0.093	MWT p=0.438
AP half-width (ms)	1.05 ± 0.09	0.89 ± 0.05	0.81 ± 0.04	0.80 ± 0.03	p=0.114	Unpaired t-test p=0.181	*p=0.032	Unpaired t-test *p=0.034	*p=0.039	MWT *p=0.009	p=0.783	MWT p=0.937
fAHP (mV)	-15.07 ± 1.10	-14.41 ± 0.98	-16.66 ± 0.69	-12.28 ± 0.80	p=0.871	Unpaired t-test p=0.661	p=0.220	Unpaired t-test p=0.234	*p=0.046	MWT *p=0.042	***p<0.001	Unpaired-t test ***p<0.001
I_h sag (mV)	0.93 ± 0.14	0.68 ± 0.12	0.56 ± 0.07	0.63 ± 0.11	p=0.645	MWT p=0.171	*p=0.047	MWT *p=0.031	p=0.118	MWT p=0.067	p=0.575	MWT p=0.742
SAAR	0.78 ± 0.02	0.82 ± 0.01	0.76 ± 0.02	0.82 ± 0.02	p=0.295	Unpaired t-test p=0.319	p=0.558	Unpaired t-test p=0.570	p=0.349	Unpaired t-test p=0.368	p=0.083	MWT p=0.080
FFAR	1.32 ± 0.06	1.33 ± 0.06	1.27 ± 0.02	1.25 ± 0.03 (n=17)	p=0.886	Unpaired t-test p=0.859	p=0.344	Unpaired t-test p=0.422	p=0.279	Unpaired t-test p=0.379	p=0.572	Unpaired t-test p=0.754
Firing frequency at 2x rheobase current (Hz)	76.66 ± 9.07	80.90 ± 7.61	96.34 ± 6.13	86.77 ± 5.80	p=0.505	Unpaired t-test p=0.722	p=0.112	Unpaired t-test p=0.093	p=0.385	Unpaired t-test p=0.341	p=0.290	Unpaired t-test p=0.275
Fmax (Hz)	142.99 ± 10.14 (n=6)	160.34 ± 12.64	157.79± 6.41	175.29 ± 9.65 (n=16)	p=0.078	Unpaired t-test p=0.381	p=0.279	Unpaired t-test p=0.296	p=0.065	Unpaired t-test p=0.078	p=0.115	Unpaired t-test p=0.124
Fss (Hz)	91.16 ± 8.28 (n=6)	98.80 ± 10.91	106.37 ± 5.39	114.46 ± 6.33 (n=16)	p=0.178	Unpaired t-test p=0.653	p=0.220	Unpaired t-test p=0.207	p=0.057	Unpaired t-test p=0.068	p=0.327	Unpaired t-test p=0.339

Table S1. sEPSCs in SST+ cells from control Vs SST+ cells from cHet mice. Related to Fig. S1

	control	cHet	LMM	Unpaired-t test or MWT
sEPSC ampl.	16.48 ± 2.57 pA (n=8, 5 anim.)	10.30 ± 1.25 pA (n=7, 5 anim.)	F=8.928 p=0.010*	Unpaired-t test p=0.016*
AUC sEPSC	88.92 ± 20.40 pA x ms (n=8, 5 anim.)	45.02 ± 3.33 pA x ms (n=7, 5 anim.) *	F=8.098 p=0.015*	MWT p=0.054
sEPSC freq.	9.47 ± 3.09 Hz (n=8, 5 anim.)	5.67 ± 1.73 Hz (n=7, 5 anim.)	F=2.261 p=0.236	Unpaired-t test p=0.202
ΔQ * f	0.91 ± 0.36 (n=8, 5 anim.)	0.25 ± 0.08 (n=7, 5 anim.)	F=5.906 p=0.030*	MWT p=0.040*
Rise time sEPSC	0.52 ± 0.05 ms (n=8, 5 anim.)	0.63 ± 0.15 ms (n=7, 5 anim.)	F=0.354 p=0.562	MWT p=0.867
Decay time sEPSC	3.91 ± 0.42 ms (n=8, 5 anim.)	3.12 ± 0.77 ms (n=7, 5 anim.)	F=1.264 p=0.281	Unpaired-t test p=0.314

Table S2. Membrane properties of BC-broad PV+ Vs BC-short PV+ in control mice. Related to Fig. 6

	BC-broad (n=21) 12 animals	BC-short (n=12) 9 animals	LMM	MWT or unpaired-t test
Resting membrane potential (mV)	-69.47 ± 0.87	-72.33 ± 1.69	F=2.511 p=0.126	Unpaired-t test p=0.108
Input resistance (MΩ)	297.14 ± 19.98	237.66 ± 19.98	F=4.830 p=0.036*	Unpaired-t test p=0.041*
Membrane capacitance (pF)	26.66 ± 1.30	33.08 ± 1.09	F=10.973 p=0.02**	MWT p=0.002**
Membrane time constant (ms)	7.95 ± 0.67	7.75 ± 0.58	F=0.042 p=0.838	MWT p=0.779
Rheobase current (pA)	123.80 ± 7.76	138.33 ± 12.42	F=1.020 p=0.323	MWT p=0.273
AP threshold (mV)	-42.11 ± 1.31	-43.38 ± 1.63	F=0.373 p=0.546	Unpaired-test p=0.558
AP amplitude (mV)	62.42 ± 1.85	61.43 ± 1.94	F=0.040 p=0.843	Unpaired-t test p=0.731
AP latency (ms)	28.63 ± 4.63	36.36 ± 7.91	F=0.871 p=0.358	MWT p=0.750
fAHP (mV)	-15.19 ± 0.67	-16.05 ± 1.06	F=0.551 p=0.464	Unpaired-t test p=0.447
I_h sag (mV)	0.77 ± 0.07	0.72 ± 0.12	F=0.093 p=0.763	MWT p=0.793
SAAR	0.75 ± 0.01	0.81 ± 0.02	F=3.644 p=0.066	Unpaired-t test p=0.074
FFAR	1.38 ± 0.03	1.31 ± 0.06	F=0.904 p=0.353	Unpaired-t test p=0.275
Firing frequency at 2x rheobase current (Hz)	75.52 ± 5.74 (n=20)	100.83 ± 7.55	F=7.082 p=0.012*	Unpaired-t test p=0.012*
Fmax (Hz)	144.58 ± 6.73 (n=16)	191.97 ± 10.48 (n=11)	F=16.315 p<0.001***	Unpaired-t test p<0.001***
Fss (Hz)	87.27 ± 5.04 (n=16)	124.23 ± 9.32 (n=11)	F=15.344 p<0.001***	MWT p=0.001**